Physical properties of intermetallic Fe$_2$VAl

by

Ye Feng

A dissertation submitted to the graduate faculty

in partial fulfillment of the requirements for the degree of

DOCTOR OF PHILOSOPHY

Major: Condensed Matter Physics

Major Professor: David W. Lynch

Iowa State University

Ames, Iowa

2001

Graduate College
Iowa State University

This is to certify that the Doctoral dissertation of

Ye Feng

has met the dissertation requirements of Iowa State University

_____
Committee Member

_____
Committee Member

_____
Committee Member

_____
Committee Member

_____
Major Professor

_____
For the Major Program

_____
For the Graduate College

TABLE OF CONTENTS

v

LIST OF TABLES

LIST OF FIGURES

ABSTRACT

Fe$_2$VAl has recently been discovered to have a negative temperature coefficient of resistivity, moderately enhanced specific heat coefficient, and a large DOS at the Fermi level by photoemission. This triggered a round of heated research to understand the ground state of this material, both theoretically and experimentally. Here we report a comprehensive characterization of Fe$_2$VAl. X-ray diffraction exhibited appreciable antisite disorder in all of our samples. FTIR spectroscopy measurements showed that the carrier density and scattering time had little sample-to-sample variation or temperature dependence for near-stoichiometric samples. FTIR and DC resistivity suggest that the transport properties of Fe$_2$VAl are influenced by both localized and delocalized carriers, with the former primarily responsible for the negative temperature coefficient of resistivity. Magnetization measurements reveal that near-stoichiometric samples have superparamagnetic clusters with at least two sizes of moments. X-ray photoemission from Fe core level shows localized magnetic moments on site-exchanged Fe. We conclude that in Fe$_2$VAl, antisite disorder causes significant modification to the semi-metallic band structure proposed by LDA calculations. With antisite disorder considered, we are now able to explain most of the physical properties of Fe$_2$VAl.

1 INTRODUCTION

I want first to give a review of the important theories and models used to describe electronic states in solids. The translational invariance of an infinite crystal decides that the wave functions of electrons are Bloch waves. Although for nano-materials and surfaces, the breakdown of periodic boundary conditions changes the electronic states appreciably at the boundary, the bulk electronic properties of most materials are well understood within this assumption.

The quantum state of electrons in solids depends on the crystal potential and electron-electron interaction. How accurately one can account for these interactions in the Hamiltonian and how tractable the mathematics is, will determine the precision of the calculations and therefore our understanding of the materials. Hartree theory, starting from the first principles, has been a tremendous step towards the understanding of the electronic states of atoms and solids. However, there are some important issues not being considered by the Hartree theory. The first one is the exchange and correlation energy. The Hartree theory treated electron-electron interactions with mean field approximations and ignored exchange interactions. The more exact Hartree-Fock formulation, with antisymmetrized many-electron wavefunctions, is unfortunately not solvable without extensive approximations. When the density of electrons becomes high, or when the wavefunction is more localized, the correlation energy becomes more significant and makes Hartree-Fock calculations extremely hard. The local density approximation (LDA), used extensively in first-principles calculations, treats exchange-correlation energy as a functional of the local electron density. This alternative formulation has gained tremendous momentum in recent years, over the Hartree-Fock approach.

The second effect of electron-electron interactions beyond the Hartree theory is screening. The effect of screening depends on the frequency and wave vector of those participating elec-

trons. For small wave vectors and slowly varying local potentials, the frequency dependence of screening is explained by the Drude theory of plasma oscillations while the Thomas-Fermi theory gives a Yukawa potential as the screened Coulomb potential. A more detailed treatment of screening by Lindhard shows oscillatory and diminishing potential at large r as $\cos{(2k_F r)}/r^3$.

Landau's Fermi liquid theory is very successful in explaining the ground-state and excited-state properties of simple materials like group I, II and noble metals. In this theory, *quasiparticles*, instead of electrons and holes, are the basic quantum entities. They are electrons renormalized by electron-electron interactions. These quasiparticles have properties very similar to those of electrons, in that they follow Fermi-Dirac statistics and have a Fermi surface. One needs to realize that the Fermi liquid theory is a phenomenological theory intended to be used only when $k_B T << E_F$.

Even though these many-body effects are already identified as the significant modifications to the Hartree theory, it is hard to incorporate them into the calculations of unknown materials, not to mention the additional perturbations due to crystal field, angular-momentum coupling, and chemical environments. Nonetheless, LDA calculation is always used as a first step to understand the unknown solids. Packaged programs like the tight-binding linear muffin-tin orbital program with atomic sphere approximation from O. K. Anderson's group [And1,And2] has been widely used by experimentalists. Ground-state total energy, partial density of states, band dispersions, and spin magnetic moments are the direct results of this self-consistent calculation. The program can be further modified to calculate surface states, phonon dispersions, optical transitions, and clusters. Of course with only exchange interaction (and some correlation interactions) considered beyond the Hartree theory, the success of this calculation is limited. It is well known that LDA calculations systematically underestimate the band gap in semiconductors and insulators, and cannot account for the band width of even simple metals.

There is one more problem when comparing the experimental data with the calculations. Unless final-state relaxation effect is negligible, the final state of a quantum measurement involves the additional excitation of other energetically near-degenerate states. Assuming Koopman's theorem, the electron eigenstates from LDA calculations can be interpreted as the

one-electron removal (or addition) energy. However, in the case of strongly correlated electronic materials, the spectral function will have to be calculated quantum-mechanically to reveal the true ground state of electrons.

Strictly speaking, the above discussion is more pertinent to band materials, in which itinerant electrons are predominant. However, in some other materials, localized electrons determine their major physical properties. In ionic insulators, the wavefunction of the electrons are very localized. The atomic aspect of the electronic states has its full manifestation, only to be modified by the crystal field. Wavefunctions constructed using molecular orbitals, or the more sophisticated many-electron configurations, are always found to be better bases to solve the relevant Hamiltonians. It is noted that in Mott-Hubbard insulators, the charge transfer from one site to another could be prohibitive due to the strong onsite electron-electron replusion, therefore effectively localizing electrons at the atomic sites. Electrons may also be localized in solids due to the randomness of the atomic potential, as in Anderson localization.

In between the itinerant and localization limit of electronic materials, there is a vast number of compounds, mostly made of transition and rare-earth metals, exhibiting rich electronic, magnetic and optical complexity. Let's first discuss why the electrons in these materials tend to have intermediate behaviors. Typically the radii of the d orbitals of the transition metals are large enough to allow direct overlap with the neighboring d orbitals, and also hybridization with sp electrons. These effects tend to delocalize the d electrons. On the other hand, the strong Coulomb interaction of additional d electrons in the same orbital, although screened by the conduction electrons, prohibits the charge transfers. The competition of these two effects are further complicated by the possible band magnetism, which is the spontaneous splitting of spin-up and spin-down bands when the Stoner condition is met. Metallic Ni, for example, has 5 electrons in the majority band and 4.46 electrons in the minority band. As a matter of fact, when the d-electron bandwidth is less than the exchange energy, it is legitimate to describe the magnetism in terms of high- and low-spin. This, of course, is a clear result of electron localization.

Lanthanide and actinide alloys are very different from the transition metals. $4f$ orbitals,

even though being the valence shell of the rare-earth elements, lie inside the $6s$ and $6p$ orbitals, within a radius on the order of 0.3 Å. This peculiarity makes $4f$ electrons more localized and less susceptible to the chemical environment. Ce compounds are even more interesting in that the hybridization energy V_{fv} between the $4f$ and valence states, $f - f$ Coulomb correlation energy U_f (Hubbard U), and single-electron energy ϵ_f of the $4f$ level with respect to E_F are all on the same order of magnitude. As a result, there is strong mixing among f^0, f^1 and f^2 states. The Anderson Hamiltonian

$$H = \sum_m \epsilon_{vm} a_{vm}^+ a_{vm} + \epsilon_f \sum_m a_{fm}^+ a_{fm} + \frac{U_f}{2} \sum_{mn} a_{fm}^+ a_{fm} a_{fn}^+ a_{fn} + V_{fv} \sum_{mn} (a_{fm}^+ a_{vn} + a_{vn}^+ a_{fm}),$$

where ϵ_{vm} is the energy of the eigenstate m of the valence band, correctly accounts for most of the physical properties of Ce. The related single-impurity Kondo problem and the Kondo-lattice problem, when the coherence effect is considered, will be elaborated later.

Another crucial aspect of solid-state physics is magnetism. Pauli exclusion principle dictates that no two electrons can be in the same quantum states. Therefore electrons tend to avoid each other via exchange interaction. It turns out that the total energy is lowered when two electrons on the same atom have parallel spins. Magnetism in solids, except Langevin diamagnetism, comes from unpaired spins. Paramagnetism of local magnetic moments gives a magnetic susceptibility inversely proportional to the temperature in the low-field or high-temperature limit. More generally, the magnetization follows a Brillouin function. Conduction electrons in the valence band can also contribute to the magnetization. The so-called Pauli susceptibility is directly proportional to the density of states at the Fermi level.

The magnetic moments in solids can either be independent of each other as in param-agnetism, or coupled together as in ferromagnetism and antiferromagnetism. The Heisenberg exchange Hamiltonian gives a good estimate of the interaction of these moments. The exchange coefficient in this Hamiltonian depends on the orthogonality of adjacent wavefunctions in the tight-binding approximation. With an increase of temperature, the coupling of moments in ferromagnetism and antiferromagnetism is gradually overwhelmed by thermal energy, giving a Curie-Weiss behavior above the critical temperature. Even if magnetic moments are not close enough to have direct interactions, there could still be coordinated magnetism of local

moments mediated by conduction electrons. It is known that screening of a charge by free electrons at large distance decays as $1/r^3$, and oscillating with a period $1/2k_F$. This, in the case of a magnetic impurity, will give a difference of spin-up and spin-down charge density of similar form. The resultant oscillatory magnetic interaction between the moments is termed the Ruderman-Kittel-Kasuya-Yosida (RKKY) interaction. It is well known that the RKKY interaction is behind both spiral arrangement of magnetic moments and spin glass.

Lastly, I want to go into some details of the Kondo effect and heavy fermion behavior. When dilute magnetic moments are embedded into a Fermi gas at low temperature, conduction electrons sometimes condense around the moment and form a singlet state with the moments of the magnetic impurity antiferromagnetically screened by the cloud of conduction electrons. This is actually a dynamic process in which conduction electrons oscillate between the Fermi gas state and Kondo state with a frequency ω_K. Typically this frequency corresponds to a "Kondo temperature" of the order of 10 K. Below this temperature, the conduction electrons are dressed by the interaction and obtain a much larger effective mass and lower mobility. Hence the name "heavy fermion." Experimentally these Kondo alloys exhibit an increase of resistivity with decreasing temperature (below the Kondo temperature) and a giant enhancement of the Pauli susceptibility at $T = 0$. It is recognized that the larger the density of states at the Fermi level or the larger the hybridization between magnetic ions and host, the higher the Kondo temperature. Because of the oscillation of conduction electrons between the Kondo state and Fermi sea, the occupation number of the conduction electrons on the magnetic ion is no longer an integer. Above the Kondo temperature, the singlet state breaks up and the moment on the impurity behaves as a localized one. When too many magnetic atoms are mixed in the alloy, the signature of a Kondo state might be overwhelmed by other magnetic interactions. However, if there is an infinite lattice with appropriate hybridization potential between the conduction electrons and the localized moments, a coherent Kondo ground state might still be achieved. It is termed a Kondo lattice state. Almost all of the Kondo lattice states are found in alloys containing lanthanide and actinide elements, especially cerium, ytterbium and uranium.

The transition metals in alloys tend to have a d orbital too delocalized to give the right combination of parameters to yield a Kondo lattice. Only recently FeSi was argued to be a Kondo lattice material [Sch1]. Both of its resistivity and magnetic susceptibility can be described by thermal activation laws with a single gap parameter (around 50 meV) in between 100 and 500 K. Its infrared conductivity shows significant reduction of Drude intensity at low temperatures. Since then extensive experimental efforts have been concentrated on this material [Hun1,Pas1,Man1,Dit1,Che1]. LDA calculations point to a nonmagnetic ground state with the Fermi level in a gap of density of states [Fuc1,Mat3,Jar1,Jar2]. Several many-body Hamiltonians have been solved for the case of FeSi, suggesting the complicated physics behind this material [Fuc2,Ris1,Ans1,Oht1,Tak1].

Another candidate is Fe_2VAl. This material was first proposed to be a $3d$ heavy fermion candidate in 1997 by Y. Nishino *et al.* [Nis1]. They observed a large decrease of resistivity with rising temperature, a moderately enhanced specific-heat coefficient, and a clear Fermi edge from photoemission. The temperature coefficient of resistivity clearly distinguished this material from typical metals. On the other hand, a crystalline semiconductor would not have a very distinct Fermi edge because of the low density of states at E_F. More than thirty papers have been published since then, speculating on the physics of this alloy. However, the detailed physics picture behind these seemingly contradictory physical properties is still elusive. This dissertation reports our experimental findings of this material. More than ten experiments have been performed covering the chemical, structural, electronic, magnetic, transport, optical, and surface properties of Fe_2VAl. Our main conclusion is that Fe_2VAl has an $L2_1$ crystal structure with large amount of antisite disorder. Most of its physical properties can be explained based on this model without evoking the Kondo phenomena.

1.1 Dissertation Organization

I will start with a literature review that focuses on the related alloys. It offers a perspective of seeing Fe_2VAl in comparison with other Heusler alloys. We published two papers in the Physical Review B, an American Physical Society journal dedicated for condensed matter

physics. They are included in this dissertation as chapters III and IV with their own literature reviews. The paper "Physical Properties of Heusler-like Fe_2VAl" stresses on the fundamental experiments of material and electromagnetic characterization. The other paper "Fe $3s$ Core-Level Splitting and Local Magnetism in Fe_2VAl" reports probing the local magnetism using x-ray photoelectron spectroscopy, and revealing for the first time, the large amount of local magnetic moments present in this material. In the end, the general conclusion chapter recapitulates the important results and their implications.

2 LITERATURE REVIEW

Fe_2VAl belongs to a group of materials called Heusler alloys. The Heusler structure has a nominal composition of X_2YZ or X_3Y, when Z=X. The atoms position themselves at $(0, 0, 0)$, $(1/4, 1/4, 1/4)$, $(1/2, 1/2, 1/2)$ and $(3/4, 3/4, 3/4)$ along the body diagonal of an fcc lattice. The Heusler structure requires the existence of inversion symmetry in the unit cell so XYXZ is the only possible body diagonal for a ternary alloy, as XXYZ will yield no inversion center. The crystal structure of the ternary XYXZ is denoted $L2_1$; while that of the binary XXXZ is $D0_3$. In XYXZ, Y and Z have full cubic symmetry while X has a tetrahedral environment. In the case of XXXZ, there are two kinds of X sites resulting in a difference of their atomic properties. In a completely disordered Heusler alloy, all sites are identical, giving a bcc lattice with half the lattice constant of the f.c.c. lattice. When one X site is empty, XYEZ forms a MgAgAs-type, or half-Heusler, structure. There are three rotations of atomic distributions that give three possible phases in half-Heusler alloys.

Heusler alloys are noted for their rich physical properties exhibited by a simple lattice structure. Ni_2MnGa has been a prototype for magnetically controlled shape-memory alloy [Ull1]. NiMnSb [Gro1] and $Co_{2-x}Fe_xMnSi$ [Fuj1] have shown interesting half-metallic ferromagnetic phases. The magneto-optic Kerr angle of half-Heusler PtMnSb is the largest of all metallic system at room temperature. UNiSn is found to be a paramagnetic narrow-bandgap semiconductor at high temperature but a metallic antiferromagnet at low temperature [Fuj2,Opp1]. First-principle calculations have shown that Fe_2VAl in the $L2_1$ structure has a nonmagnetic ground state, although two out of four atoms are typically magnetic [Guo1,Sin1,Weh1,Ban1]. Heusler alloys have long been a test bed for more detailed understanding of the electronic band structure and magnetism. That is the reason why we were set to study Fe_2VAl back in 1997.

Fe$_2$VAl is commonly studied together with other Fe$_{3-x}$V$_x$Al alloys. They are obtained by substituting Fe with V. A good understanding of the parent compound Fe$_3$Al, its isoelectronic Fe$_3$Ga, its isomorphous Fe$_3$Si, and Fe$_2$VGa will benefit our discussion on Fe$_2$VAl.

Fe$_3$Al has a $D0_3$ structure. As early as 1932, Bradley and Jay [Bra1] have recognized the structural disorder in this material, in terms of Fe-Al site interchange. Recently, Fultz *et al.* [Ful1] calculated the partial density of phonon states of completely disordered, partially disordered, and ordered Fe$_3$Al with the atomic distribution measured by the Mössbauer experiments. They are found to be in excellent agreement with the results from inelastic nuclear resonant scattering. The dominance of short-range order in the phonon density of states is established. These experiments demonstrated that antisite disorder is intrinsic in the growth of Fe$_3$Al. Ti, V, Cr, and Mn has been mixed into Fe$_3$Al to substitute for Fe [Nis3]. Lattice contraction was found for both Cr and V, on which Nishino *et al.* based their claim that Fe$_2$VAl alloy forms at the minimum of lattice constants. Since the (111) and (200) diffraction peaks of the $D0_3$ phase was also observed in their experiments, they concluded that V occupies the octahedral Fe site to give an $L2_1$ Fe$_2$VAl. As we shall see in Chapter III, even the XXYZ type of atomic arrangement can give x-ray diffraction peaks at the same positions as the (111) and (200) reflections of the $D0_3$ structure. The actual x-ray diffraction profile is very complicated and demands a lot of modeling before a full explanation is at hand.

Fe$_{4-x}$Si$_x$, which is ferromagnetic with a $D0_3$ structure for $0 < x < 1$, has been well studied and understood [Nic1,Nis2] using a local environment model. In this model, the moment of the Fe with octahedral symmetry is always 2.2 μ_B; while that of the Fe with tetrahedral symmetry is roughly proportional to the number of nearest-neighbor Fe atoms, being around 1.2 μ_B in Fe$_3$Si. Theoretical calculations with the coherent potential approximation [Kud1] showed that the partial density of states of d electrons can be easily described in terms of crystal-field orbitals and local binding, therefore vindicating the local environment model. Indeed, the calculated moments found excellent agreement with experiments. When another $3d$ transition metal element substitutes for Fe in Fe$_3$Si, site preference is clearly marked [Nic1,Kud1]. The elements to the left of Fe replace the Fe having cubic symmetry; while those to the right of Fe

replace the Fe having tetrahedral symmetry. The local-environment model [Nic1,Kud1] works amazingly well even in these pseudo-binary alloys. The *ab-initio* calculations revealed another interesting result. It is first found by Kudrnovsky *et al.* [Kud1] that in both $Fe_{4-x}Si_x$ and $Fe_{3-x}V_xSi$, Si has almost no contribution to the density of states at the Fermi level.

Fe_3Ga has an $L1_2$ structure. A slight substitution for Fe by either Cr, Mn, Co, or Ni will result in a $D0_3$ structure with strong site selection [Kaw2,Nis3], as in Fe_3Si.

Fe_2VGa has the same number of valence electrons as Fe_2VAl. Band structure calculations, assuming that Fe_2VGa has the $L2_1$ type structure with VFeGaFe along the diagonal, yielded a similar semimetallic ground state [Weh1]. The only important difference seems to be a larger band overlap in the DOS near E_F. Experimentally Endo *et al.* [End3] found giant (transverse) magnetoresistance (GMR) of 44% in this material, with a magnetic field of 6 T. The Curie temperature of Fe_2VGa is 15 K. The resistivity has a broad maximum around the Curie temperature, similar to that of Fe_2VAl. The authors attributed the GMR to the moment alignment due to the magnetic field. When more Fe is replaced by V, the negative resistivity slope is more pronounced, which is different than Fe_2VAl. Their magnetization measurements on Fe_2VGa reported a spontaneous magnetization much larger than ours of Fe_2VAl. Recognizing that the residual magnetization might come from the formation of magnetic clusters due to sample inhomogeneity, they made a rough estimate of the density of the magnetic clusters. Their cluster density of 1.3% for Fe_2VGa is about an order of magnitude larger than ours for Fe_2VAl, which is consistent with the larger spontaneous magnetization in Fe_2VGa. We found satisfactory agreement in the physical properties of these two materials.

Our own LDA calculation predicts a ferromagnetic ground state for Fe_2VSi; but this is not found experimentally. Above Néel temperature 123 K, Fe_2VSi has an effective moment of 1.87 μ_B and a Weiss temperature of -212 K [End2]. Below 123 K, an antiferromagnetic state with 0.22 μ_B per Fe atom is established. It is surprising to notice that in another study, only a *Curie* temperature was identified in $(Fe_{1-x}V_x)_3Si$ with $0 < x < 0.2$ [Nis2]. This difference suggests possible spin fluctuation in Fe_2VSi.

The transport properties of related Heusler alloys are also discussed in chapter III. We

can indeed find an intricate interplay of structure, electronic ground state, magnetism, and transport in these materials.

3   PHYSICAL PROPERTIES OF HEUSLER-LIKE Fe$_2$VAl

Ye Feng[2], J. Y. Rhee[3], T. A. Wiener[2], D. W. Lynch[2], B. E. Hubbard[4], A. J. Sievers[4], D.L. Schlagel[5], T. A. Lograsso[5], and L. L. Miller[5]

Abstract

A comprehensive characterization of the compound Fe$_2$VAl was carried out. Samples grown by arc melting or the Bridgman method have Al and Fe deficiencies of up to 5 at.%. Czochralski-grown samples were Fe rich and Al deficient. X-ray diffraction implies appreciable antisite disorder in all of our samples. Fourier-transform infrared (FTIR) spectroscopy measurements showed that the carrier density and scattering time had little sample-to-sample variation or temperature dependence for near-stoichiometric samples. FTIR and dc resistivity suggest that the transport properties of Fe$_2$VAl are influenced by both localized and delocalized carriers, with the former primarily responsible for the negative temperature coefficient of resistivity. Magnetization measurements reveal that near-stoichiometric samples have superparamagnetic clusters with at least two sizes of moments. We conclude that in Fe$_2$VAl, antisite disorder causes significant modification to the semimetallic band structure proposed theoretically. With antisite disorder considered, we are now able to explain most of the physical properties of Fe$_2$VAl. None of our data suggest heavy- fermion behavior in our samples.

[2]Ames Laboratory and Department of Physics and Astronomy, Iowa State University, Ames, Iowa 50011
[3]On leave from Department of Physics, Hoseo University, Asan, Choongnam 336-795, Korea
[4]Laboratory of Atomic and Solid State Physics, Cornell University, Ithaca, NY 14853-2501
[5]Ames Laboratory, U. S. D. O. E., Ames, Iowa 50011

3.1 Introduction

Fe$_2$VAl has a number of properties that make it of current interest. Its high resistivity and negative temperature coefficient of resistivity (TCR, defined as $d(\ln R)/d$T) distinguish it from conventional intermetallic compounds[Nis1]. Yet, contrary to an intermetallic semiconductor, photoemission experiments on Fe$_2$VAl suggest a reasonable density of states (DOS) at the Fermi level E_F [Nis1,Sod1]. The electronic specific-heat coefficient was also reported to be enhanced[Nis1,Lue1,Kat1]. Despite the presence of Fe, this Heusler alloy does not order ferromagnetically, at least above 4.2 K[Nis1,Pop1], although some samples show evidence of superparamagnetism (SPM)[Pop1].

As V is doped into the Heusler alloy Fe$_3$Al with the fcc $D0_3$ structure, no abrupt structural transformation is observed[Nis1,Pop1]. There have been different nomenclatures for the resultant Fe$_2$VAl to imply structural information. In this paper, we use Fe$_2$VAl as the name of the stoichiometric compound. FeVFeAl and FeFeVAl are used to indicate the basis along the body diagonal in the $D0_3$ unit cell. In FeVFeAl, V has replaced the Fe which has O_h site symmetry in Fe$_3$Al, resulting in the cubic $L2_1$ structure. If all the V atoms interchange with the same neighboring Fe atoms in FeVFeAl, the basis becomes FeFeVAl. In fact, FeFeVAl and FeVFeAl are the only two possible $D0_3$ bases in Fe$_2$VAl.

Several band-structure calculations have been carried out[Guo1,Sin1,Weh1,Ban1], all of which found FeVFeAl to be a nonmagnetic semimetal with a low carrier concentration, about one electron and hole for each 350 unit cells. The DOS of FeVFeAl at E_F is about 0.1/eV per f.u.[Weh1]. For comparison, the calculated DOS at E_F of FeFeVAl and Fe$_3$Al are about an order of magnitude larger than that of FeVFeAl[Guo1]. Fe atoms, when placed on the V sites, carry local moments of 1.8 μ_B in FeFeVAl[Guo1], 2.2 μ_B in various Fe$_{2+x}$V$_{1-x}$Al supercells[Sin1] and 3.0 μ_B in near-stoichiometric Fe$_2$VAl[Ban1]. These papers, however, gave different opinions on the transport properties and effective-mass enhancement at E_F. Guo et $al.$[Guo1] excluded electron-phonon coupling and expected spin fluctuations in FeVFeAl to be the main cause of the enhanced effective mass, while the negative TCR was due to carrier localization. Singh and Mazin[Sin1] argued that magnetic moments, due to nonstoichiometry

and antisite defects, may be responsible for a large effective mass and the complex transport properties from low-density carriers interacting with localized magnetic moments. Weht and Pickett[Weh1] proposed dynamic correlations between holes and electrons as responsible for the resistivity. Bansil *et al.*[Ban1] treated the substitution of Fe with V within the coherent-potential approximation. Recognizing the possibility of samples' having stoichiometry problems and antisite defects, they stated that Fe_2VAl may have the character of a heavy fermion material.

In the following we report a variety of measurements on several samples of Fe_2VAl. Our measurements include composition (by atomic emission spectroscopy), infrared reflectance, X-ray diffraction (XRD), magnetization, and conductivity measurements. None of the samples were exactly stoichiometric due to the preferential loss of Al and Fe in arc melting, and composition gradients in the Bridgman and Czochralski growths. In both FeVFeAl and FeFeVAl, the (111) reflection should be present in the XRD patterns for an fcc lattice, but in all patterns reported here, this reflection is found to be very weak. We modeled the XRD patterns by several possible antisite structures and show that certain site interchanges can account for the weakened (111) peak, although a unique crystal structure cannot be determined. The infrared (IR) spectra can be described accurately by Lorentzian oscillators representing the IR-active phonons, a single Drude term representing either electrons or holes, and a high-frequency dielectric constant. Magnetization measurements with varying field and temperature confirmed the existence of SPM. The anomalous dc resistivities, although influenced by the magnetic states of the samples, are largely caused by antisite disorder. The Boltzmann formalism of conduction breaks down because of the very short mean free paths of the carriers. Localization due to site disorder, compounded with the low density of carriers in the ordered phase, is responsible for the very large residual resistivity and negative TCR. We found that Fe_2VAl samples grown from the above methods are not single-phase Heusler alloys with the FeVFeAl structure. Their physical properties are the direct result of this deviation.

3.2 Samples and Experiments

Polycrystalline samples were grown by arc-melting (samples $\mathcal{A}1$ and $\mathcal{A}2$). Samples $\mathcal{B}1$ and $\mathcal{B}2$ were grown by the Bridgman method. We also obtained some single-crystal samples grown by the Czochralski method[Tal1] (sample $\mathcal{C}$). Sample $\mathcal{A}1$ was repeatedly melted on a water-cooled copper hearth with a partial pressure of argon, starting from high-grade Fe, V and Al. The ingot was kept at 1273 K for two days. It was then cut in half and further annealed at 1273 K for 1 h and 673 K for 4 h. Sample $\mathcal{A}2$ was similarly arc melted and then annealed at 1073 K for two days before cutting. The weight loss was 0.8% for $\mathcal{A}1$ and 1.0% for $\mathcal{A}2$. Optical samples from $\mathcal{A}1$ and $\mathcal{A}2$ were further annealed for 12-17.5 h at 673 K to remove surface strain due to mechanical polishing. We studied the effect of annealing in arc-melted samples with magnetization and resistivity measurements. The individual histories of samples are listed in Table 3.1.

For the growth of the Bridgman sample, Fe, V and Al (99.5% or better) were arc melted into buttons then drop cast into a chilled copper mold. The crystal was grown from the as-cast ingot in an alumina crucible. To reduce the Al vaporization during crystal growth the furnace was backfilled to 3.4 atm with argon running through an in-line gettering furnace after the chamber and sample had been outgassed at 773 K. The sample was kept at 1923 K for 1 h to allow thorough mixing before being withdrawn from the hot zone at 5.5 mm/h. Heat treatment of the sample was one week at 1273 K, followed by 4 h at 673 K. $\mathcal{B}1$, from the tip of the single crystal, shows better-defined spots in Laue patterns than $\mathcal{B}2$, which was cut from further along the ingot.

Chemical analysis using inductively coupled plasma atomic-emission spectroscopy (ICP-AES) was performed. XRD experiments used Cu K_α I and II lines in Debye-Scherrer geometry. Reflectance measurements were made down to 20 meV at room temperature using a Nicolet FTIR spectrometer, and down to 5 meV at 4 K using a Bomem (FTIR) spectrometer with a 4.2 K Si bolometer detector. The electrical resistivity was measured from 1.8 K to 300 K using a standard four-probe technique. Due to the uncertainty of the bar dimensions and the contact separation, there is an approximate uncertainty of $\pm$ 10% in the absolute values. dc

magnetization was measured using a commercial SQUID magnetometer.

3.3 Chemical Characterization

The ratios of atomic emission intensities are tabulated in Table 3.2. In most of the near-stoichiometric samples, an Fe and Al deficiency relative to V is clear. Comparing the total masses estimated from the integrated intensity of atomic emission with those weighed before the ICP-AES experiments, all samples suffer about 2% weight loss in the preparation of solutions, except for $\mathcal{A}1$ with its 5% weight loss and some white precipitate in the solution. The precipitate presumably consists of an impurity from the crystal, or Al_2O_3. The vapor pressures of Al and Fe at 1273 K, the annealing temperature, are 10^{-4} and 10^{-6} Torr, respectively, and that of V is negligible. The loss of Al and Fe in arc-melted ingots could very well be from their preferential evaporation in the growth process and in the high-temperature annealing. Assuming there is no loss of V, the above atomic ratios translate to weight losses of 1.6% for $\mathcal{A}1$ and 2.6% for $\mathcal{A}2$. These ICP-AES atomic ratios tend to overestimate the loss, when compared to the weight loss after the arc-melting growth. We suspect the arc-melted Fe_2VAl samples were already Fe and Al deficient right after growth. Bridgman sample $\mathcal{B}1$ is off stoichiometry but $\mathcal{B}2$ looks reasonable. This difference arises from the interplay of the temperature gradient from the pedestal to the melt, and the convective and diffusive mixing that are particular to the Bridgman method. Although the stoichiometry of $\mathcal{B}1$ is quite different from those of the others, we keep it in our study for comparison. The Czochralski sample is Fe rich. This deviation is presumably also from the crystal growth. We regard all samples except $\mathcal{B}1$ and $\mathcal{C}$ to be be near stoichiometric. Although Al and Fe deficiencies will cause a shift of E_F, it is considered to be insignificant. Scanning electron microscope studies show that both the polished and unpolished surface of sample $\mathcal{A}2$ are homogeneous within 5 at.%.

3.4 Powder X-ray Diffraction

In the history of Fe_2VAl characterization, different structures have been proposed, based on powder XRD results. Early research on $FeAl_{1-x}V_x$ [Okp1] identified the formation of

FeVFeAl through powder XRD and neutron scattering. Few guesses of possible structures were used to settle on this structure. Nevertheless, the agreement between theory and experiment appeared to be excellent. Later, Popiel *et al.* [Pop1] attempted to obtain the occupation-number distribution for every constituent at every site of the $D0_3$ structure from experimental powder XRD. Few details were provided for this complicated process but they concluded that V prefers to be in the FeFeVAl ordering, rather than FeVFeAl. They also noticed that the ratio of structure factors for (111) to (200) reflections decreased throughout the $Fe_{3-x}V_xAl$ series with increasing x, reaching about 0.2 at Fe_2VAl. Structural disorder was suggested. Recently, Nishino *et al.* [Nis1] claimed Fe_2VAl to be FeVFeAl, although diminished (111) and (200) peaks were also reported. Here we present our data and analysis to show that FeVFeAl is not the only crystal structure in Fe_2VAl, and the suppression of the (111) and (200) peaks can be explained by structural disorder.

We used the PowderCell 2.1 program [Nol1] and an experimental lattice constant of 5.761 Å to calculate peak intensities for all structures considered, with a Debye-Waller factor of 0.9 for each atom. In ideal FeVFeAl, the strongest peaks have Miller indices of (220), (422), (400), (200), and (111), shown in Fig. 3.1. The calculated intensity ratios $F^2_{(111)}/F^2_{(220)}$, $F^2_{(200)}/F^2_{(220)}$, $F^2_{(400)}/F^2_{(220)}$, and $F^2_{(422)}/F^2_{(220)}$ are 0.043, 0.065, 0.133, and 0.229, respectively. Although in our calculations $F^2_{(111)}/F^2_{(220)}$ agrees very well with the calculated and experimental value in Ref. [Okp1], our calculated $F^2_{(200)}/F^2_{(220)}$ is 0.065 instead of the 0.5 reported for both calculations and experiments[Okp1].

All our experimental XRD profiles (of $\mathcal{A}1$, $\mathcal{A}2$, $\mathcal{B}1$, $\mathcal{B}2$, and $\mathcal{C}$) were similar and none showed any unexpected peaks above the 1% detection limit. Measured patterns of samples $\mathcal{A}2$ and $\mathcal{B}1$ are shown in Fig. 3.1, along with the calculated patterns for FeVFeAl and FeFeVAl. Peak heights were normalized to that of the (220) peak which was given an intensity of 100. All measured spectra show a (111) peak at about $2\theta \simeq 27°$ with strongly suppressed intensity, and a (200) peak slightly reduced from the calculated values for FeVFeAl, at $2\theta \simeq 31°$.

In addition, the patterns from samples $\mathcal{A}1$, $\mathcal{A}2$, $\mathcal{B}2$, and $\mathcal{C}$ had shoulders on the low-angle sides of the (220), (400) and (422) peaks, but sample $\mathcal{B}1$ had almost no such shoulder.

(Since the ICP-AES analysis showed $\mathcal{B}1$ to be chemically different from others, we should note that about 10% chemical disorder may not distort the diffraction pattern noticeably.) These shoulders scaled in intensity with their respective main peaks, indicating a close connection in origin. We also annealed some powder from $\mathcal{A}1$ at 673 K for 30 h, and powdered part of the annealed optical sample $\mathcal{A}2$. In both cases, the lower-angle shoulders of the diffraction peaks were no longer visible. Therefore, these shoulders probably originated from the bulk, not from the grinding process. However, the $F^2_{(111)}/F^2_{(200)}$ ratio of $\mathcal{A}1$ becomes even smaller after annealing.

We did numerical fitting to our XRD data to obtain relative peak intensities. A fourth-order polynomial was used to fit the background, which was then subtracted. Assuming a Lorentzian lineshape for each peak, we acquired the intensity ratios of $F^2_{(111)}/F^2_{(220)}$ and $F^2_{(200)}/F^2_{(220)}$ and tabulated them in Table 3.3. We also used two Lorentzians for the (220) peaks. $\frac{F^2_{(200)}}{F^2_{(220)L}}$ and $\frac{F^2_{(200)}}{F^2_{(220)H}}$ in the table refer to ratios to the shoulders at lower angles and to the main peaks at higher angles of the (220) peaks. It is noted that $F^2_{(111)}$ and $F^2_{(200)}$ scale better with the main peak or the total of (220), rather than with just the shoulder. For all samples except $\mathcal{B}1$, we also found $\frac{d_{220,L}}{d_{220,H}} = \frac{d_{400,L}}{d_{400,H}} = \frac{d_{422,L}}{d_{422,H}}$, where d_{hkl} is the spacing between planes with Miller index of (hkl).

Since most of the peak ratios roughly agree with the predicted values for FeVFeAl, we assign all our samples to be close approximates to this structure. However, the shoulders and the reduced (111) and (200) intensities require some modification to the structure. Since the FeFeVAl phase enhances the (111) peak relative to the (200) peak (see Fig. 3.1 and Table 3.4), its presence does not explain our XRD profiles. The calculated effect of vacancies did not agree with experiments either. Within the structure of FeVFeAl, reducing the atomic form factor of Al by 10% increased both (111) and (200) intensities with respect to that of the (220), while reducing the Fe form factor increased the (111) intensity and reduced that of the (200).

We consider site-interchange disorder as the possible cause of the weakened (111) peak. Instead of constructing many supercells to model antisite disorder, we treated each lattice site as being statistically occupied. With no indication of a structural transition[Nis1,Pop1], it is

Table 3.1 Annealing histories of arc-melted samples.

Samples	Annealing Process
$\mathcal{A}1$	@1273 K (48 h + 1 h after cutting) and @673 K (4 h)
$\mathcal{A}1$-optical	@1273 K (48 h + 1 h after cutting), @673 K (4 h),
	and @673 K (12 h) after polishing
$\mathcal{A}2$-5a, 5b, 5c, 5d	@1073 K (48 h)
$\mathcal{A}2$-5b-ANN	$\mathcal{A}2$-5b further annealed @673 K (30 h)
$\mathcal{A}2$-optical, 2b, 2c	@1073 K (48 h) and @673 K (17.5 h)
$\mathcal{A}2$-2c-ANN	$\mathcal{A}2$-2c further annealed @1273 K (1 h)
	and various anneals below 723 K

Table 3.2 ICP-AES results for Fe_2VAl samples. The standard deviations are given in brackets in the first column.

Atomic Ratio	$\mathcal{A}1$	$\mathcal{A}2$	$\mathcal{B}1$	$\mathcal{B}2$	$\mathcal{C}$
Fe/2V (3.3%)	0.99	0.96	0.90	0.98	1.05
Al/V (3.0%)	0.95	0.98	0.83	0.99	0.98

Table 3.3 Experimental XRD intensity ratios with standard deviations in brackets.

Sample	$\dfrac{F^2_{(111)}}{F^2_{(200)}}$	$\dfrac{F^2_{(200)}}{F^2_{(220)tot}}$	$\dfrac{F^2_{(200)}}{F^2_{(220)L}}$	$\dfrac{F^2_{(200)}}{F^2_{(220)H}}$
$\mathcal{A}1$	0.44(10%)	0.033(3%)	0.11(9%)	0.045(4%)
$\mathcal{A}2$	0.37(5%)	0.032(2%)	0.12(6%)	0.041(2%)
$\mathcal{C}$	0.27(32%)	0.030(7%)	0.091(11%)	0.043(8%)
$\mathcal{B}2$	0.30(18%)	0.048(5%)	0.21(18%)	0.062(8%)
$\mathcal{B}1$	0.33(13%)	0.036(3%)	0.17(18%)	0.045(6%)
$\mathcal{A}1$ [a]	0.26(17%)	0.052(5%)	-	-

[a]Powder from sample $\mathcal{A}1$ further annealed at 673 K for 30 h.

Table 3.4   All the theoretical structures considered for antisite disorder and the ratios of powder pattern intensities. In the "Atomic arrangement" column the sequence is $(0,0,0)$ -$(\frac{1}{4},\frac{1}{4},\frac{1}{4})$ -$(\frac{1}{2},\frac{1}{2},\frac{1}{2})$ -$(\frac{3}{4},\frac{3}{4},\frac{3}{4})$. **FA**=Fe/Al, **FV**=Fe/V, and **VA**=V/Al. See the text for explanations.

Space group	Atomic arrangement	$\dfrac{F^2_{(111)}}{F^2_{(200)}}$	$\dfrac{F^2_{(111)}}{F^2_{(220)}}$	$\dfrac{F^2_{(200)}}{F^2_{(220)}}$
$Pm(-3)m$ [a]	Fe-**VA**-Fe-**VA**$^{\alpha *}$	0.000	0.000	0.065
$Pm(-3)m$[a]	**FV**-**FA**-**FV**-**FA**$^{\beta *}$	0.000	0.000	0.021
$Fd(-3)m$	**FV**-**FA**-**FA**-**FV**	∞	0.021	0.000
$Fd(-3)m$	**VA**-Fe-Fe-**VA**$^{\gamma}$	∞	0.064	0.000
$Fm(-3)m$	Fe-V-Fe-Al$^{\delta}$ [b]	0.650	0.043	0.065
$Fm(-3)m$	**FV**-Al-**FV**-Fe	3.750	0.080	0.021
$Fm(-3)m$	**FA**-V-**FA**-Fe *	0.270	0.006	0.021
$F(-4)3m$	Fe-Fe-Al-V [c]	4.020	0.085	0.020
$F(-4)3m$	**FV**-**FV**-Al-Fe	1.520	0.060	0.040
$F(-4)3m$	**FA**-**FA**-V-Fe	8.050	0.024	0.003
$F(-4)3m$	Fe-**VA**-**FV**-**FA***	0.071	0.003	0.040
$F(-4)3m$	Fe-**VA**-**FA**-**FV**	13.000	0.040	0.003
$F(-4)3m$	**FV**-**VA**-**FA**-Fe	∞	0.043	0.000
72.6% of α and 27.3% of γ		0.37	0.017	0.047
70.9% of β and 29.1% of δ		0.37	0.013	0.034

[a]Its proper lattice constant is half of 5.761 Å
[b]This is the FeVFeAl phase mentioned in the text
[c]This is the FeFeVAl phase mentioned in the text

reasonable to assume that the underlying lattice for Fe_2VAl is the $D0_3$ structure, with basis atoms at $(0, 0, 0)$, $(\frac{1}{4}, \frac{1}{4}, \frac{1}{4})$, $(\frac{1}{2}, \frac{1}{2}, \frac{1}{2})$ and $(\frac{3}{4}, \frac{3}{4}, \frac{3}{4})$. At each basis site, we assumed fractional occupation by Fe, V and Al in units of $\frac{1}{2}$ atom. With few exceptions, the diffraction intensities for non-half-integer occupancy can be interpolated from those with half-integer occupancy. This choice of quantization reveals the necessary features of the diffraction pattern without extensive calculations. We assumed full stoichiometry for the model structures.

We can categorize the structures by the number of sites with identical occupancy and determine the crystal symmetry, or space group, through site-symmetry analysis[Fat1]. There are 13 possible atomic arrangements that keep the proper stoichiometry, all listed in Table 3.4. When two atoms A and B share the same site, the label A/B is used. We calculated all the peak intensities and normalized them. Because of a sum rule[Okp1], the intensities of the (220), (400), and (422) peaks of these 13 structures were identical, hence not useful for discrimination.

Only four types of structures can yield a reduced $F^2_{(111)}/F^2_{(200)}$. They are starred in Table 3.4. Any one, or several, of these can mix with FeVFeAl or other phases with high $F^2_{(111)}/F^2_{(200)}$ values, to produce a powder pattern close to the experimental one. They may also produce the observed shoulders because of the slightly different lattice parameters of the phases involved. The XRD profile is then a weighted average of that of each phase. The bottom two rows in Table 3.4 list two phases that can give an $F^2_{(111)}/F^2_{(200)}$ of 0.37, the average of $\mathcal{A}1$, $\mathcal{A}2$, and $\mathcal{B}2$.

So far we have established antisite structural disorder as the probable reason for the distorted XRD patterns and that annealing at 673 K does not restore the FeVFeAl structure, although the XRD shoulders are reduced or eliminated. We have not yet been able to pinpoint exactly what lattice structure our samples have. The major difficulties are due to the vast number of possibilities for antisite substitutions in a ternary compound and similar scattering form factors of Fe and V. We do not know how much a role non-diffracting phases, if any, play in the overall picture. It is not surprising to find such large antisite disorder in arc-melted Heusler alloys. XRD of the line-phase compound Fe_3Al revealed a structural disorder of 8%[Bra1]. Mössbauer experiments on Fe_3Al [Ful1] and $(Fe_{1-x}V_x)_3Al$ [Pop1] with $0 \leq x \leq 0.6$ confirmed

this antisite disorder and showed it persisting over the V alloying process.

3.5   FTIR Results

Reflection spectroscopy around the plasma edge is well recognized as an accurate measure of carrier density and scattering time for metallic alloys and semiconductors. Typically the dielectric function of metals is composed of a constant ϵ_∞ and contributions from free electrons, phonons, and interband transitions. ϵ_∞ accounts for the contributions from interband transitions at higher energies.

Figure 3.2 shows the reflectance $R(\omega)$ of $\mathcal{A}1$, $\mathcal{A}2$, $\mathcal{B}1$ and $\mathcal{B}2$. (Because of the small size of sample $\mathcal{C}$, we were not able to measure it.) There are two peaks around 0.03 eV and 0.045 eV in all samples. Besides these two peaks, a tiny feature is also seen around 0.04 eV in $\mathcal{A}2$, which shifts to lower energies with decreasing temperature. Bridgman sample $\mathcal{B}1$ has an additional peak around 0.06 eV. There is no significant change in $R(\omega)$ of $\mathcal{A}2$ from 4 K to 300 K, suggesting similar Drude contributions at all temperatures. Other samples, except $\mathcal{B}1$, seem to have similar carrier densities and scattering times. Recent optical conductivity measurements show that Fe_2VAl has interband transitions peaking at 1.1 eV, with a threshold above the Drude contribution around 0.1 eV. [Oka1,Fen1] We therefore tend to regard the upturn of $\mathcal{A}2$ and $\mathcal{B}2$ near 0.08 eV as the onset of interband contributions.

The peaks at 0.03 and 0.045 eV are readily identified as phonon peaks for the following reasons. First, inter-valence-band transitions depend strongly on the available states below and above E_F. At infrared frequencies, the strength of these transitions is strongly influenced by thermal broadening of the Fermi function. If the 0.03-eV peak were due to interband transitions, its intensity and width would have changed significantly when the temperature increases from 4 to 300 K. Optical phonons are, however, much less temperature sensitive. Second, it is not unusual that disorder changes energy eigenstates near E_F thereby altering the frequency, width or intensity of interband transitions. With all of the peaks aligning in energy and having similar width and intensity (numerically shown in Table 3.5), we believe that both peaks are of phonon origin, not from inter-valence-band transitions.   Third,

IR radiation excites transverse optical (TO) phonons of certain symmetry at the Brillouin zone center according to dipole selection rules. Correlation-method[Fat1] analysis applied to FeVFeAl with space group $Fm(-3)m$ results in two doubly-degenerate TO modes with $\mathbf{F}_{1u}$ symmetry which are IR active. A third doubly degenerate TO mode has $\mathbf{F}_{2g}$ symmetry and is Raman active but not IR active. In contrast, the FeFeVAl with space group $F(-4)3m$ has three IR active phonon modes with $\mathbf{F}_2$ symmetry. The survival of these phonon features in the presence of structural disorder hints at the dominance of FeVFeAl-like regions in all near-stoichiometric Fe_2VAl samples.

To understand these spectra quantitatively, we fit each $R(\omega)$ with a sum of a Drude term for the free carriers and Lorentz oscillators for the phonons, together with a constant ϵ_∞. Since only one Drude term was needed to yield a good fit, we will mention only the electronic carriers later on, although holes can as well be present or dominant. Carrier densities and scattering times can be determined, assuming a free-electron mass. Two Lorentz oscillators for samples $\mathcal{A}1$, $\mathcal{A}2$ (at 4 and 300 K) and $\mathcal{B}2$, and three for $\mathcal{B}1$, were used in the fitting process. The fit was excellent for all samples except for the minor feature around 0.04 eV in $\mathcal{A}2$. The best-fit parameters are listed in Table 3.5. The self-consistency of this fitting is confirmed on sample $\mathcal{A}2$ by comparing the optical conductivity calculated with its best-fit parameters and that from a Kramers-Kronig transformation of its full-range $R(\omega)$[Fen1], in which only $R(\omega)$ below 0.02 eV and above 22 eV were extrapolated. It should be pointed out that assuming a constant ϵ_∞ is appropriate, as optical conductivity data[Oka1,Fen1] show negligible interband transitions below 0.1 eV.

The fitting results confirmed that the carrier concentrations of $\mathcal{A}1$, $\mathcal{A}2$ at 4 and 300 K, and $\mathcal{B}2$ are similar. Their average at 300 K, $3.5 \times 10^{20}/cm^3$, agrees with that reported in Ref. [Oka1]. The carrier density for $\mathcal{A}2$ at 300 K is 0.017 electrons/f.u., comparable to the 0.024 carriers/f.u. [Sin1] and 0.006 carriers/f.u. [Weh1] predicted from first-principles calculations, although these calculations yielded a renormalized mass for the carriers. It is precisely because of the low density of carriers that the TO phonons are not well screened.

Despite the significantly larger carrier density of $\mathcal{B}1$, scattering times for all samples are

close to 1.0 $\times 10^{-14}$ s, a typical time scale for metals at room temperature. However, similar scattering times at 4 K and 300 K indicate that the scattering is not due to phonons. The product of carrier concentration and scattering time of $\mathcal{A}2$ becomes a bit larger from 300 K to 4 K, over which the resistivity increases by almost a factor of two, as shown in Sec.3.7. This fact requires another mechanism of transport besides the conventional conduction described by the Boltzmann formulation to account for the *change* of resistivity over temperature.

Variations in ϵ_∞ come from the dielectric response of valence electrons at higher energies. If we take ϵ_∞ to be 200, an average number in Table 3.5, we can estimate the position of the mean oscillator representing all valence electrons. With 24 valence electrons/f.u. contributing to this oscillation,

$$\omega_0 = \sqrt{\frac{4\pi e^2 n}{m\epsilon_\infty}} = 1.9 \text{ eV}.$$

This is fairly consistent with the position of the main peak of the optical conductivity at 1.1 eV from our spectroscopic ellipsometry[Fen1].

Lastly, we report that no pseudogap due to electron correlation is observed in this material. Most of the pseudogaps in strongly correlated materials, as in a similar $3d$ metallic alloy FeSi[Sch1,Dam1,Che1], have a strong temperature dependence in reflectivity and optical conductivity. In contrast, our FTIR data for Fe_2VAl show that the concentration and scattering time of free carriers remain nearly constant when the temperature is changed. These electronic carriers do not appear to be influenced by any temperature-dependent correlation mechanisms.

3.6   Magnetism

The magnetization and magnetostatic susceptibilities of our Fe_2VAl samples are shown in Figs. 3.3 and 3.4, respectively. Magnetization was measured up to 5.5 T at 2 K and susceptibility from 2 K to 350 K in 0.1 T for all samples. For $\mathcal{B}2$, magnetization was also measured at 30 K.

In Fig. 3.3, $\mathcal{A}1$ and $\mathcal{C}$ have saturation moments between 0.3 and 0.4 μ_B/f.u. Their susceptibilities in Fig. 3.4 show a magnetic transition temperature near 20 K for $\mathcal{A}1$ and 50 K for

$\mathcal{C}$. The susceptibility of sample $\mathcal{A}1$ above 20 K cannot be explained by the Curie-Weiss law. However, sample $\mathcal{C}$ shows clear Curie-Weiss behavior with μ_{eff}=2.8 μ_B/f.u., T_C=53 K, and χ_0=-8.5 $\times 10^{-6}$ emu/g, when susceptibility above 70 K is fitted with

$$\chi = \chi_0 + \frac{N_{f.u.}\mu_{eff}^2}{3k_B(T - T_C)}.$$

The stoichiometry measurement shows that sample $\mathcal{C}$ is iron rich. The excessive Fe atoms might occupy the V or Al sites and form ferromagnetic clusters. Nishino *et al.*[Nis1] have also observed in their resistivity data that a slight increase of iron content in Fe_2VAl does result in ferromagnetism.

All $\mathcal{A}2$-derived samples, even annealed at low temperature, have paramagnetic-like magnetizations, as shown in Fig. 3.3. They do not saturate up to 5.5 T. The magnitude of magnetization of these samples is more than an order of magnitude smaller than those of $\mathcal{A}1$ and $\mathcal{C}$. There is no hysteresis observed within the limit of the instruments. The lack of hysteresis is considered a signature of paramagnetism or SPM. Above the blocking temperature T_B, the coupling of SPM clusters is overwhelmed by the thermal energy, giving a magnetization described well by Brillouin functions with large effective magneton numbers. These $\mathcal{A}2$-derived samples all appear to have T_B less than 2 K. The inverse susceptibility data of these samples cannot be explained by the Curie-Weiss law with a single slope at high temperature. Temperature might have an effect on the size of the SPM clusters or the weak interaction among them, to cause this complicated magnetic behavior.

Additional annealing at 673 K does not change the magnetic properties of Fe_2VAl in a significant way. The susceptibility of samples $\mathcal{A}2$-5b-ANN is reduced compared to $\mathcal{A}2$-5b but with no new features. However, $\mathcal{A}2$-2c, after being heat treated at 1273 K for 1 h, shows enhanced susceptibility and magnetization, by a factor of 10 or more. Sample $\mathcal{B}2$ has most of its characteristics similar to those of $\mathcal{A}2$-derived samples, although from the susceptibility a magnetic transition around 10 K is visible. It appears that $\mathcal{A}2$-2c-ANN and $\mathcal{B}2$ are in intermediate magnetic states between those of $\mathcal{A}2$ and $\mathcal{A}1$. These different states probably have variations in local stoichiometry, the size of SPM clusters, or coupling among them. The field-dependent resistivity, shown later in Sec.3.7, also suggests the magnetic transformation

from $\mathcal{A}2$, $\mathcal{B}2$, to $\mathcal{A}1$.

Popiel *et al.*[Pop1] pointed out the existence of SPM in $Fe_{3-x}V_xAl$ alloys. Across $Fe_{3-x}V_xAl$, they found through Mössbauer and magnetostatic experiments that, with an increase of V content, ferromagnetism weakens and SPM becomes prevalent for $x > 0.6$. The reported magnetization of $Fe_{2.2}V_{0.8}Al$ has a similar shape and magnitude as those of our sample $\mathcal{A}1$, albeit a large difference in T_B. (Our susceptibility data are to be multiplied by a field of 0.1 T before comparing with their magnetization data.) They reported the moments of SPM clusters vary from 10 μ_B to $10^4\mu_B$, according to different isotherms of magnetization. Fitting our magnetization-vs-field data with one Brillouin function was unsuccessful. Using two Brillouin functions, or even better, two Langevin functions,

$$\frac{\sigma - \sigma_0}{\sigma_S} = a[\coth(\frac{\mu_1 H}{k_B T}) - \frac{k_B T}{\mu_1 H}] + (1-a)[\coth(\frac{\mu_2 H}{k_B T}) - \frac{k_B T}{\mu_2 H}]$$

we were able to obtain an excellent fit, permitting the extraction of the moments μ_1 and μ_2, their relative fractions, a and $1-a$, the average moment μ_{avg} [$\mu_{avg} = a\mu_1 + (1-a)\mu_2$], the total saturation magnetization σ_S, the field-independent magnetization σ_0, and the cluster density σ_S/μ_{avg}. The results of these fits are listed in Table 3.6.   The field-independent magnetization σ_0, $3 \times 10^{-3}\mu_B$/f.u., correponds to a susceptibility of 9×10^{-5} emu/g, which is on the same scale as the high-temperature tail of the susceptibility. Because the Pauli susceptibility is field independent and almost temperature independent, it is probably the cause for the σ_0 and the observed tail.

The concentrations of those two clusters are about constant throughout all $\mathcal{A}2$ samples. Annealing $\mathcal{A}2$-5b reduces the moments of both clusters but enhances the cluster density. Sample $\mathcal{B}2$ has about the same cluster fraction as $\mathcal{A}2$ but with a larger cluster moment. However, at 30 K it has predominantly one type of cluster with 11 μ_B/cluster. Recently the field-dependent specific heat of Fe_2VAl was successfully treated with two-level Schottky fits[Lue1]. An effective magnetic moment of 3.7 μ_B per cluster and a cluster density of 0.0037/f.u. was reported below 8 K. These numbers are comparable to ours, obtained from isothermal magnetization measurements. But we have identified two kinds of SPM clusters with about equal concentration at 2 K.

Table 3.5   FTIR reflectivity fitting parameters.

	$\mathcal{A}1$	$\mathcal{A}2$	$\mathcal{A}2$	$\mathcal{B}2$	$\mathcal{B}1$
temperature (K)	300	4	300	300	300
carrier density (10^{20}/cm^3)	5.0	2.0	2.2	3.3	25
scattering time (10^{-15}s)	7.9	13	11	9.6	7.4
ϵ_∞	184	158	96.3	246	300
phonon E1 (meV)	29.5	29.6	29.7	29.9	30.1
E1 width (meV)	0.79	1.1	1.0	2.8	1.5
phonon E2 (meV)	45.3	45.6	45.4	46.0	45.8
E2 width (meV)	1.3	1.9	1.8	3.5	1.5
phonon E3 (meV)					61.4
E3 width (meV)					4.3
intensity ratio I_{E1}/I_{E2}	3.9	3.8	4.1	2.7	3.4

Table 3.6   Results of a two-cluster Langevin fit. Magnetic moments (μ_1, μ_2, μ_{avg}) are in units of μ_B, fraction of clusters (a) that have μ_1 in percentage, magnetizations (σ_0, σ_S) in 10^{-3} μ_B/f.u., and cluster density σ_S/μ_{avg} in per f.u.

Sample	T	μ_1	a	μ_2	μ_{avg}	σ_0	σ_S	$\frac{\sigma_S}{\mu_{avg}}$
$\mathcal{A}$2-2b	2 K	37	39%	3.1	16	4.6	24	0.0015
$\mathcal{A}$2-2c	2 K	8.0	55%	1.6	5.1	2.7	20	0.0039
$\mathcal{A}$2-5a	2 K	17	43%	2.7	8.9	2.5	21	0.0024
$\mathcal{A}$2-5b	2 K	26	34%	3.2	11	2.3	21	0.0019
$\mathcal{A}$2-5d	2 K	23	40%	3.3	11	2.6	24	0.0022
$\mathcal{A}$2-5b-ANN	2 K	13	44%	2.5	7.1	4.8	21	0.0030
$\mathcal{B}$2	2 K	71	46%	4.3	35	4.6	53	0.0015
$\mathcal{B}$2	30 K	547	7%	11	48	7.1	48	0.0010

3.7   Resistivity

Resistivities of all our samples are shown in Fig. 3.5. The resistivity of $\mathcal{B}1$ increases with temperature, typical of metallic alloys. $\mathcal{A}1$ has a large residual resistivity, a peak at 18 K, and monotonically decreasing resistivity at higher temperature. The temperature of the peak matches very well with its T_B. The resistivity of sample $\mathcal{C}$ has a similar shape but with a much larger residual and overall resistivity. It peaks at 50 K, in accord with the change of its susceptibility with temperature. The increase of resistivity below T_C of sample $\mathcal{C}$ and T_B of sample $\mathcal{A}1$ is apparently due to magnetic scattering. For all the samples derived from $\mathcal{A}2$, resistivity is marked by a negative TCR and lack of peak structure, in line with the fact that their T_B's are below 2 K. At very low temperature, the resistivities of all $\mathcal{A}2$ samples depart from their almost linear trend. It will be shown later that this upward departure is related to magnetic ordering. Sample $\mathcal{B}2$ has a resistivity almost overlapping that of $\mathcal{A}2$-5b.

The fact that two bars, $\mathcal{A}2$-5c and $\mathcal{A}2$-5d, from the same bulk sample show resistivity differences of almost a factor of two reveals a homogeneity problem, although magnetostatic measurements have yielded fairly consistent results for all $\mathcal{A}2$-derived samples. Various groups have produced quite different resistivity data for arc-melted samples[Nis1,Mat1,End1]. The cleaved arc-melted ingots show visible grain boundaries inside the bulk, which might account for part of the resistivity difference. More importantly, the antisite disorder in Fe_2VAl is very sensitive to annealing and other conditions under which samples are prepared. It is interesting to note the correlation of the high-temperature susceptibility and the overall magnitude of resistivity in $\mathcal{A}2$-2b, 5b, 5d, and 5b-ANN, *i.e.*, the larger the susceptibility, the smaller the resistivity. This may be due to the difference in density of states at E_F, which resulted in a concomitant change of Pauli susceptibility and conductivity.

The resistivity measured before annealing at 673 K ($\mathcal{A}2$-5b) is smaller than that after annealing ($\mathcal{A}2$-5b-ANN). Matsushita *et al.*[Mat1] have established that how a sample of Fe_2VAl is cooled from an anneal at 1073 K will determine the magnitude of its resistivity. We want to stress that their anneal is different from our additional low-temperature anneal.

We also measured resistivity vs. temperature down to 4 K in a 5.5 T magnetic field (Fig.

3.6). The resistivities of $\mathcal{A}1$, $\mathcal{A}2$-2b, and $\mathcal{B}2$ were all suppressed in the field, but only at low temperature. The peak of $\mathcal{A}1$ was shifted to around 40 K and considerably broadened. The suppression of the resistivity of $\mathcal{A}2$-2b with applied field indicates the magnetic origin of its upward tail at low temperature. The resemblance of these two sets of data around the bifurcation point, with and without magnetic field, suggests the same kind of residual magnetic ordering, *i.e.*, the magnetic moments of $\mathcal{A}2$-2b responded to the applied magnetic field the same way as in $\mathcal{A}1$ just above T_B. $\mathcal{B}2$ did not show an appreciable field dependence until around 25 K. In this case, a resistivity maximum was formed, even though without field no maximum was observed. Samples $\mathcal{A}2$, $\mathcal{B}2$ and $\mathcal{A}1$ give a unique set of resistivity data on the magnetic scattering in the presence of external magnetic fields. The suppression of resistivity and the shift or formation of a peak at higher temperature in magnetic fields are both consistent with the field alignment of the spins of SPM clusters, thus making the lattice more ordered for transport and making it harder to thermally break the ferromagnetic alignment of the SPM clusters. The magnetic transformation of $\mathcal{A}2$, $\mathcal{B}2$ to $\mathcal{A}1$ found here echos our results from the magnetic susceptibility.

Now we try to assess our resistivity data quantitatively, according to possible theoretical models. Several references[Nis1,End1] modeled Fe$_2$VAl as a narrow-gap semiconductor. We fitted our resistivity with $\rho = \rho_{const} + \rho_0 \times e^{\frac{\Delta E}{k_B T}}$. Between 240 and 300 K, ΔE was 0.015 eV for $\mathcal{A}1$ and $\mathcal{A}2$-2b. For all other samples except $\mathcal{B}1$, the activation energy ΔE was 0.025 - 0.035 eV. Endo[End1] reported a semiconducting gap of 0.07 eV which is close to our gap, $2\Delta E$. However, this gap can not be taken as exact since the temperature may not be proper to treat the electrons as a nondegenerate gas. The infrared reflectance spectra are also inconsistent with a real semiconducting band gap. In the case of a 0.06-eV band gap, carriers would be frozen at 4 K by the Fermi-Dirac distribution and cause a significant drop of the free-electron concentration. Below 25 K, we can fit the upward resistivity to an energy gap of less than one tenth of a meV. We dismiss this gap at low temperature as not physically meaningful because the Fermi-Dirac distribution at 2 K easily overwhelms it. Besides, SPM was shown to be related to this upward trend, casting doubt on its electronic origin.

Other physics is possible behind this activation energy of tens of meV. But first, we need to realize that the Boltzmann formulation for conduction is not appropriate for Fe_2VAl. From our FTIR data, the mean free path $(v_F\tau)$ for electrons is 27 Å at 4 K and 24 Å at 300 K. With an electron wavelength $2\pi/k_F$ around 34 Å, we cannot use the semi-classical Boltzmann equation and assume the phase memory of electrons is lost in the scattering process. We have to treat this problem using the more general Kubo-Greenwood and multiple-scattering formulations.

Bergmann[Ber1] first pointed out that weak localization through multiple scattering and quantum interference can give an additional contribution to electron localization. This effect is relatively strong when the scattering length is short. Raising the temperature will cause electrons to collide with phonons inelastically, thereby losing coherence, enhancing the conductivity. Weak localization can produce a negative TCR. On the other hand, the application of a magnetic field introduces a relative phase shift of $2e\Delta\phi/\hbar$, which normally destroys the constructive interference and enhances the conductivity. We did not find much change of resistivity with a field of 5.5 T for most of the temperature range in which a negative TCR was observed. We therefore regard weak localization not to be the primary mechanism causing the negative TCR in Fe_2VAl.

Large amounts of disorder in amorphous semiconductors will create mobility edges at the band tails. Beyond the mobility edge, the carrier contribution to the conductivity is nominally zero. The DOS of FeVFeAl calculated from first principles can be split into two subbands above and below E_F due to the crystal field and metallic bonding[Sin1,Weh1,Ban1]. With a large amount of antisite disorder introduced, a mobility edge on each of the two subbands will be formed right above and below E_F, leaving the states in between localized. The DOS between these two mobility edges will increase with more disorder, filling the void of the pseudogap. The mobility edges will also move toward the centroids of the subbands with more disorder. A rise of temperature will cause more delocalized states above the upper mobility edge and below the lower mobility edge to be involved in the conduction process, giving a negative TCR. This conduction process will probably not cause changes in the Drude term in the IR due to its short mean scattering time and strong damping. But it is possible that the large density

of states at E_F, as seen in the photoemission and specific-heat measurements, comes from localized states.

It is interesting to notice that a negative TCR is prevalent in $Fe_{4-x}Si_x$ for $0 \leq x \leq 1$[Nis2], $(Fe_{0.8}M_{0.2})_3Si$ with M=V, Mn, Cr, Ni, Co[Nis2], $(Fe_{1-x}V_x)_3Si$ for $0 \leq x \leq 0.2$[Nis2], $(Fe_{1-x}Co_x)_3Si$ for $0 \leq x \leq 0.6$[Nis2], $(Fe_{1-x}V_x)_3Ga$ for $0 \leq x \leq 0.3$[Kaw1], $(Fe_{1-x}Ti_x)_3Ga$ for $0 \leq x \leq 0.3$[Kaw1], and $(Fe_{1-x}V_x)_3Al$ for $0 \leq x \leq 0.35$[Nis1]. Recently Zarek *et al.*[Zar1] reported that Fe_2VAl in a simple cubic lattice also shows a negative TCR between 4.2 K and 300 K. With only FeVFeAl in a semimetallic ground state, the negative TCR in these alloys may have little to do with semimetallicity. Mooij[Moo1] studied the transport properties of a number of transition-metal alloys finding that high resistivity with concomitant negative TCR was a "universal" property of many. Disordered phases were noted for more effectively creating negative TCR than their ordered counterparts. Putting impurities into pure metals can create a negative TCR. For example, doping up to 33% Al into pure Ti induced a transition from a positive to a negative TCR. The temperature span of this negative TCR was very wide for many alloys. An important conclusion was drawn that the transport properties of these alloys have little dependence on crystal structures or band structures. We think the intrinsic disorder of the Heusler structure is the likely cause of the negative TCR of the above alloys.

Mooij[Moo1] set a room-temperature resistivity of 150 $\mu\Omega$cm as the universal criterion for the sign of TCR; if the room temperature resistivity of a sample is larger than this value it is likely to have a negative TCR. Later, Tsuei[Tsu1] collected more data and concluded that Mooij's criterion was based on too small a data set and that the "universal criterion" of 150 $\mu\Omega$cm is *not* universal. He also argued that the nonuniversality of the Mooij correlation is mostly attributed to the competition between the quantum-mechanical effects of incipient localization and classical Boltzmann electron transport. However, there is still a unique and monotonic correlation between the TCR and resistivity for a specific disordered metallic system. The crossover resistivity, ρ_c, from negative to positive TCR is not universal to all materials, but dependent upon the individual material characteristics. ρ_c is given by [Tsu1]

$$\rho_c = \rho_B\left(0\right)\left[1 - \frac{3}{\left(k_F l_e\right)^2} + \frac{6.75}{\left(k_F l_e\right)^4}\right]^{-1},$$

where

$$\rho_B\left(0\right) = \frac{3\pi^2\hbar}{e^2 k_F^2 l_e},$$

the Boltzmann resistivity at $T = 0$ K and l_e is the elastic mean free path. Since actual numerical analysis [Tsu1] reveals a fairly linear relation between the TCR and the resistivity near and below zero TCR, we plot our samples' TCR-vs-resistivity at 150 and 273 K in the inset of Fig. 3.5. From linear regression we get ρ_c=492 and 342 $\mu\Omega$cm at 150 and 273 K, respectively. Both are larger than the value suggested by Mooij. If we use $k_F = 1.8 \times 10^7$ cm^{-1} from our FTIR analysis, l_e is 11.4 Å at 150 K and 14.2 Å at 273 K. These values are about half the l_e's obtained from the FTIR data analysis. Since we did not measure a series of samples with various levels of disorder, we could not claim that these values have a firm physical meaning. Nevertheless, this analysis gives us at least a clear understanding that the disorder in Fe$_2$VAl alloys plays an important role in many physical properties.

Without the interference of magnetic ordering in Fe$_2$VAl samples at low temperature, the residual resistivity (ρ_{RES}) would be the almost-linearly-temperature-dependent resistivity extended to 0 K. Understanding ρ_{RES} in these Heusler alloys, without the complication due to the anomalously large magnetic scattering[Nis2,Kaw1] present, should shed some light on this negative TCR. The ρ_{RES} of (Fe$_{1-x}$V$_x$)$_3$Ga, (Fe$_{1-x}$V$_x$)$_3$Si, and (Fe$_{1-x}$V$_x$)$_3$Al are plotted in Fig. 3.7. The data points have been taken from Ref. [Nis1] for (Fe$_{1-x}$V$_x$)$_3$Al, Refs. [Nis2] and [End2] for (Fe$_{1-x}$V$_x$)$_3$Si, Refs. [End1] and [Kaw1] for (Fe$_{1-x}$V$_x$)$_3$Ga.

Work on Fe$_3$Si$_{1-x}$Al$_x$[Mui1] yielded considerable insight on the effect of disorder in Heusler alloys. It was found that Al-Fe site disorder can be assumed to be proportional to the amount of Fe$_3$Al present in Fe$_3$Si, resulting in a linear relation of ρ_{RES} and x. The Si-Al disorder scattering has a parabolic dependence on x, vanishing at x=0 and x=1. In Fig. 3.7, the ρ_{RES} of (Fe$_{1-x}$V$_x$)$_3$Si and (Fe$_{1-x}$V$_x$)$_3$Ga can be similarly understood in terms of Fe$_3$Si, Fe$_2$VSi, Fe$_3$Ga, and Fe$_2$VGa. The resistivity induced by Fe-V disorder in these two series can be estimated to be of the order of 100 $\mu\Omega$cm. The distortion of the parabolic shape in (Fe$_{1-x}$V$_x$)$_3$Ga is obvious, with the peak position moving to x=0.25. The gross shape of ρ_{RES} vs. x of (Fe$_{1-x}$V$_x$)$_3$Al seems to contradict the above simple model of antisite disorder. However, in the following

we shall see that the ρ_{RES} of $(Fe_{1-x}V_x)_3Al$ can be approximated as well by the homogeneous mixing of Fe_3Al and Fe_2VAl with intrinsic disorder in both compounds.

The linear dependence of ρ_{RES} on x between end-point compounds has a root in percolation theory. When two media are mixed homogeneously and each makes a closed circuit, we have in effect two resistors in parallel. Assuming

$$R_1 = \frac{\rho_1 l}{xA}, \ and \ R_2 = \frac{\rho_2 l}{(1-x)A},$$

one gets

$$\rho_{tot}(x) = \frac{\rho_2 \rho_1}{\rho_1 + (\rho_2 - \rho_1)x},$$

where x is the volume fraction of the phase with resistivity ρ_1. When ρ_1 and ρ_2 are not very different, $\rho_{tot}(x)$ is almost a straight line connecting the endpoints. This is indeed the case in $Fe_3Si_{1-x}Al_x$, $(Fe_{1-x}V_x)_3Si$ and $(Fe_{1-x}V_x)_3Ga$. But when there is a large difference between ρ_1 and ρ_2, as in the case of Fe_3Al and Fe_2VAl, the above formula gives an upward curvature, similiar to our experimental data. Shown in the inset of Fig. 3.7 is the experimental ρ_{RES} with that from percolation mixing of end-point compounds subtracted. It is observed that the difference curve for $(Fe_{1-x}V_x)_3Al$ has a parabolic shape with even more distortion than that for $(Fe_{1-x}V_x)_3Ga$. We think the shift of the "parabolic" peak is probably related to stronger multiple scattering due to electron localization. Although it is very crude to assume that $(Fe_{1-x}V_x)_3Al$ is a simple mixture of Fe_3Al and Fe_2VAl with Fe-V disorder considered additionally, there are experimental indications of a continuous ferromagnetism-to-SPM transition from Fe_3Al to Fe_2VAl[Pop1].

3.8 Summary

Through our investigation, Heusler-like Fe_2VAl is regarded as having mostly the FeVFeAl structure but with severe antisite disorder. This leads to large deviations of physical properties from the theoretical speculations based on the ideal FeVFeAl structure. Magnetically, SPM clusters form out of antisite disorder. However, not all antisite disorder results in the formation of SPM clusters. If we assume each disordered FeVFeAl formula unit contributes an average of

$2\,\mu_B$, with the available data on saturation magnetization and ferromagnetic coupling assumed, there are about only 1-2% of the formula units in SPM states. The moments of Fe atoms in other disordered cells are probably locked in a spin-glass or antiferromagnetic state with no average moment.

The electronic structure of Fe_2VAl is not strongly perturbed by antisite disorder except near E_F. The DOS can be decomposed into two parts. The FeVFeAl phase has a DOS predicted from first-principles calculations. This phase is the origin of the observed Drude conductivity. The disordered phase has a large DOS near E_F and these states are localized. Away from E_F, there are delocalized electrons and holes on the far sides of the mobility edges. With E_F falling in the gap of the DOS of itinerant carriers, the mobile free-carrier density is small and has little temperature dependence. However, with an increase of temperature, more delocalized carriers from the disordered phase are involved in the conduction process, giving a negative TCR. The very large ρ_{RES} of Fe_2VAl is due to the low density of carriers in the ordered phase and the freezing of delocalized carriers in the disordered phase. With most of the DOS at E_F from localized states, the intensity of Fermi-edge photoemission[Nis1] and the specific-heat coefficient are enhanced in Fe_2VAl relative to the ordered phase. Recent resonant photoemission experiments found that the partial DOS calculated from first principles depicts the valence band of Fe_2VAl very well, except near E_F [Sod1]. This finding is in qualitative agreement with our assignment of the DOS as well. We found no evidence in these samples for heavy-fermion behavior.

We can make a simple comparison of the electronic properties of Fe_2VAl and amorphous Si. With similar DOS's, the negative TCR in Fe_2VAl results from the same physics that caused the resistivity to drop with increasing temperature in amorphous Si. The optical-absorption edge in amorphous Si is not very sharp and falls off exponentially according to Urbach's rule because of the transitions from and to the tail states. Optical conductivity of similar shape near the onset of interband absorption is also observed in Fe_2VAl.
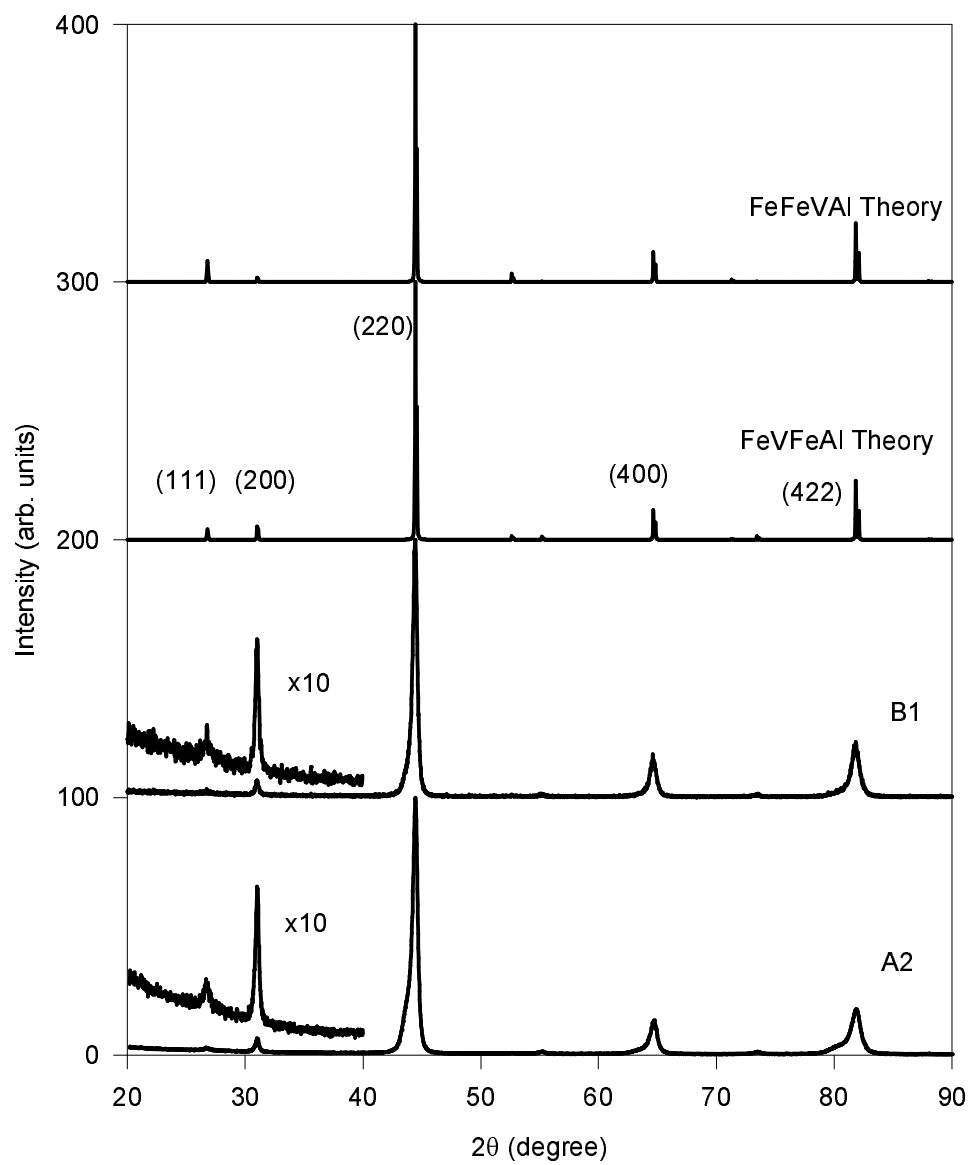
Acknowledgments

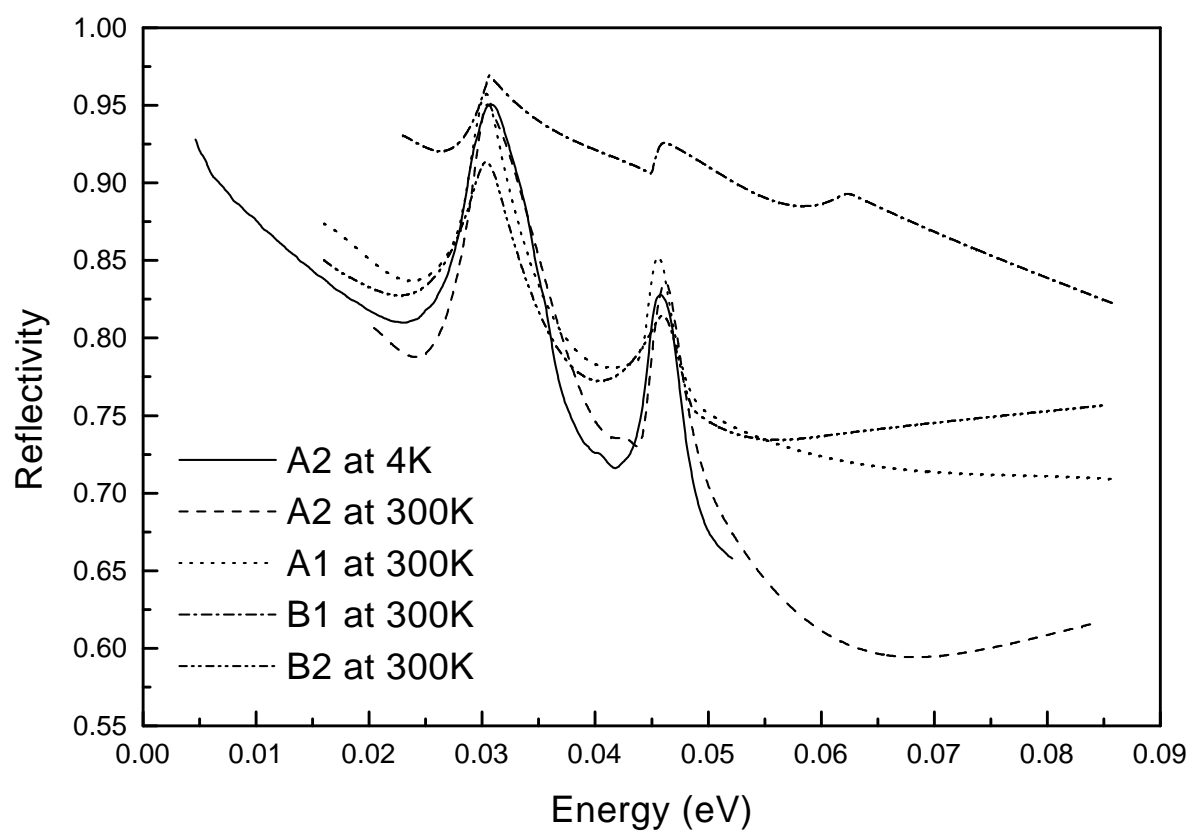Figure 3.1   Powder XRD patterns of Fe$_2$VAl.

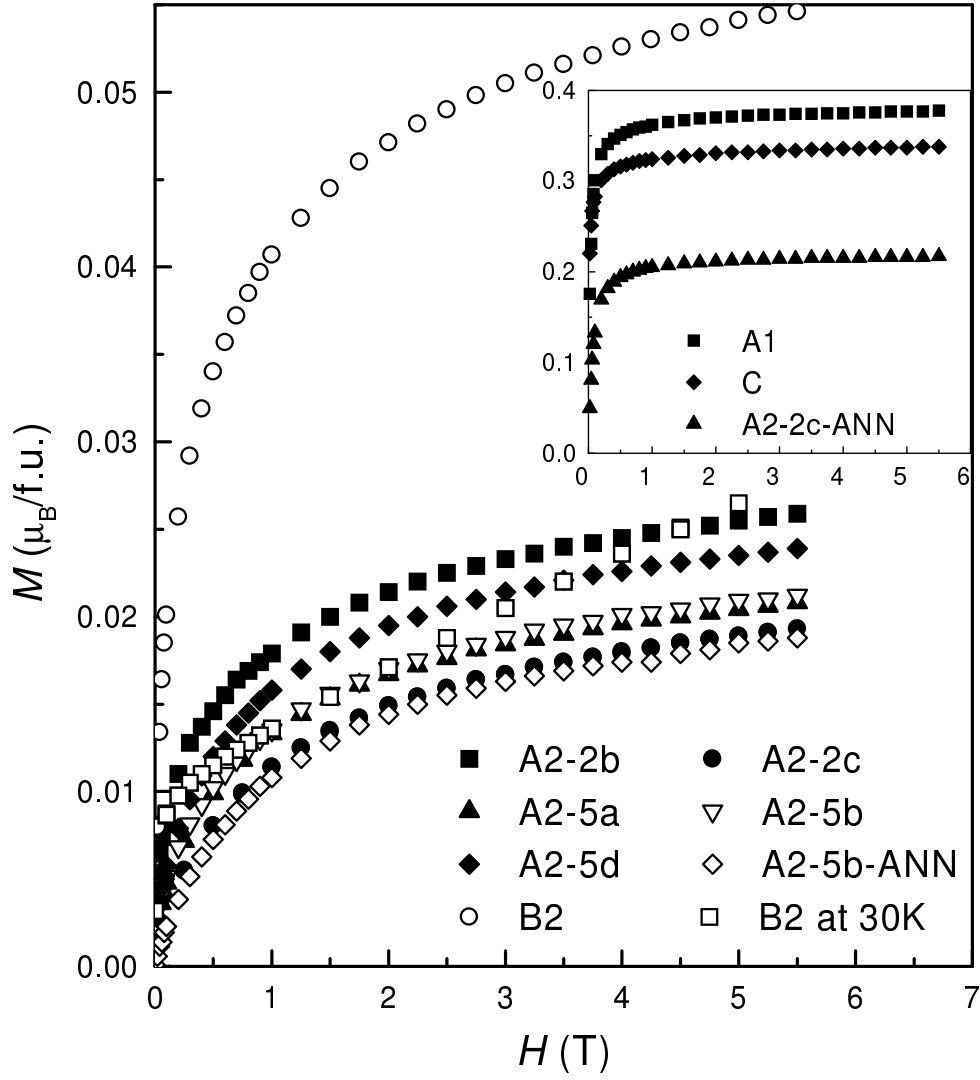Figure 3.2   Far-IR reflectivity of Fe$_2$VAl.

Figure 3.3   Magnetization of Fe_2VAl measured at 2 K unless otherwise specified.
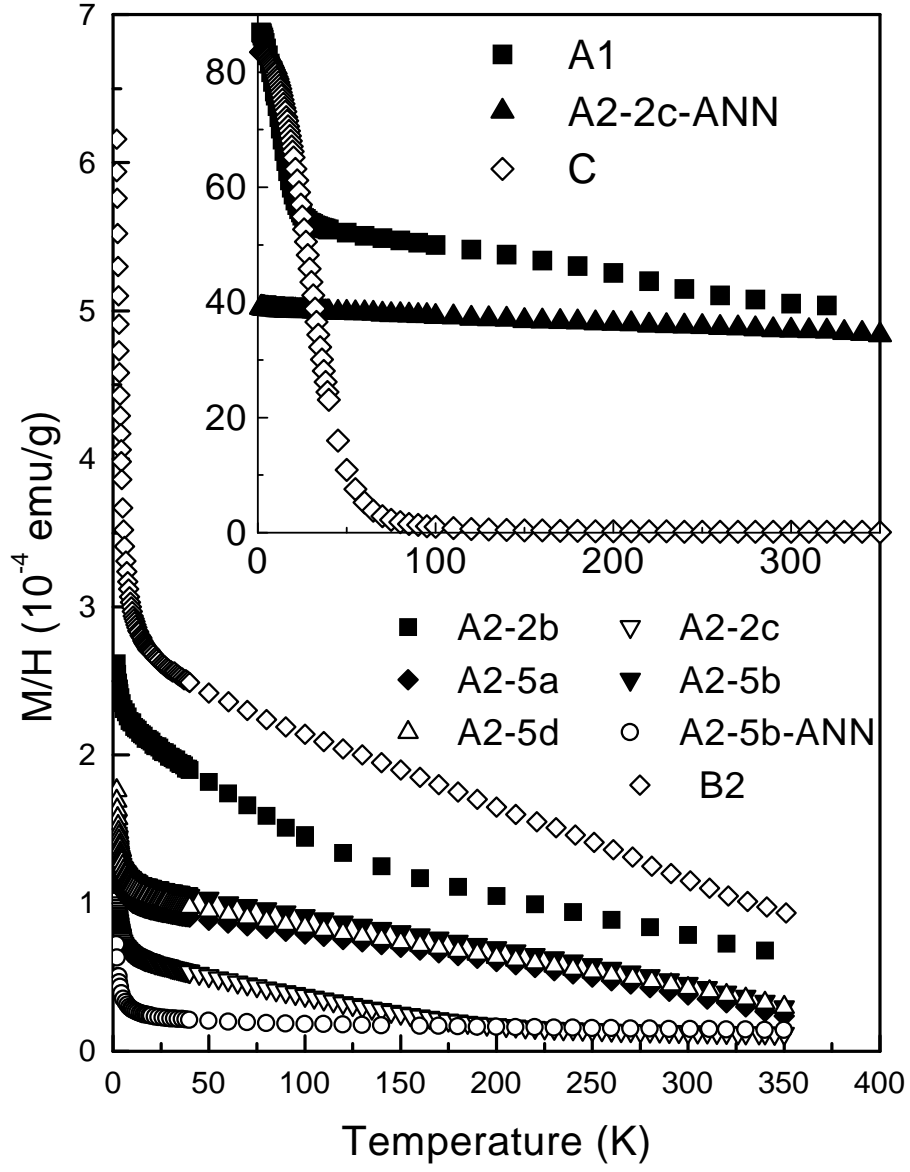
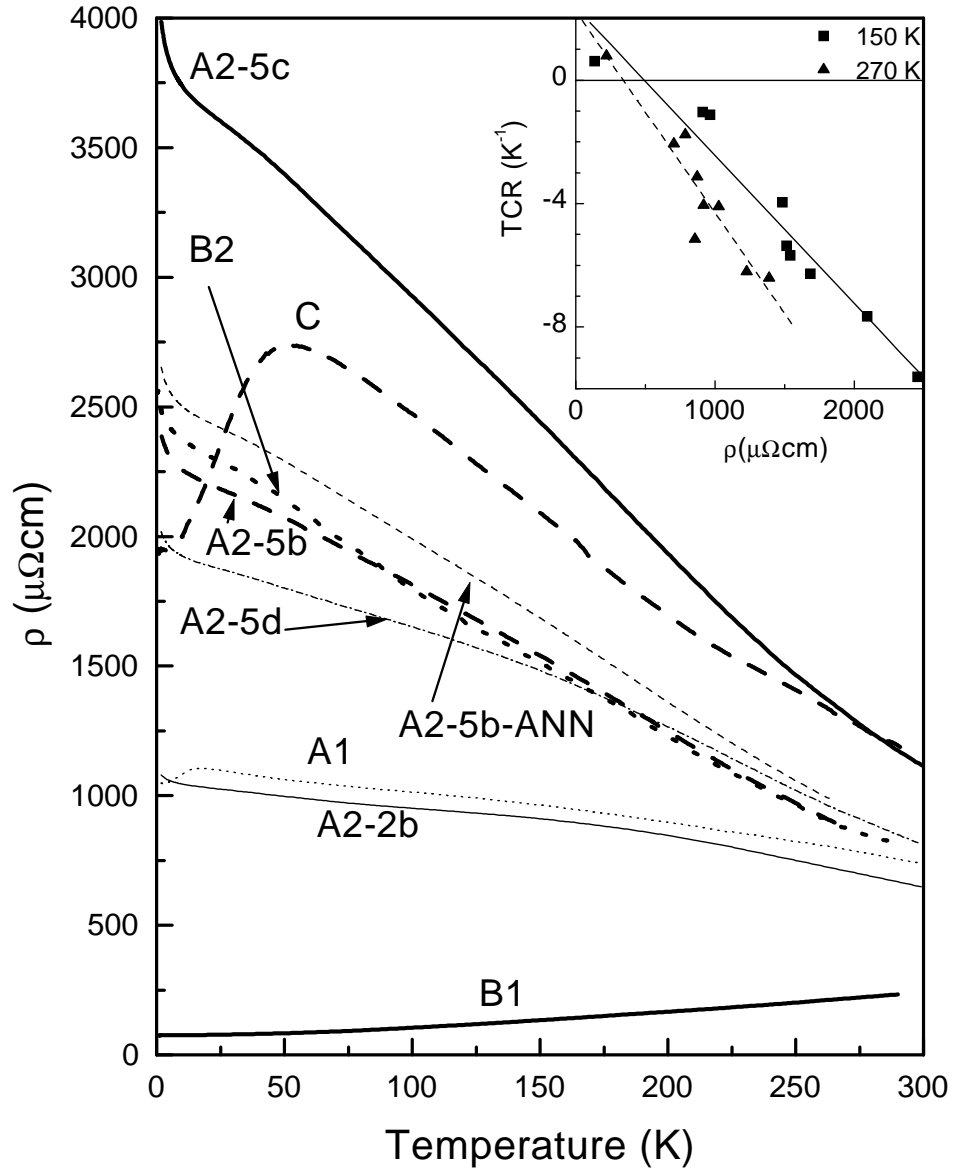Figure 3.4 Susceptibility of Fe_2VAl measured at 1 kG.

Figure 3.5 Resistivity of Fe$_2$VAl. Inset shows the correlation of TCR and resistivity at $T = 150$ K and 273 K. The solid and dashed lines are results of linear regressions.
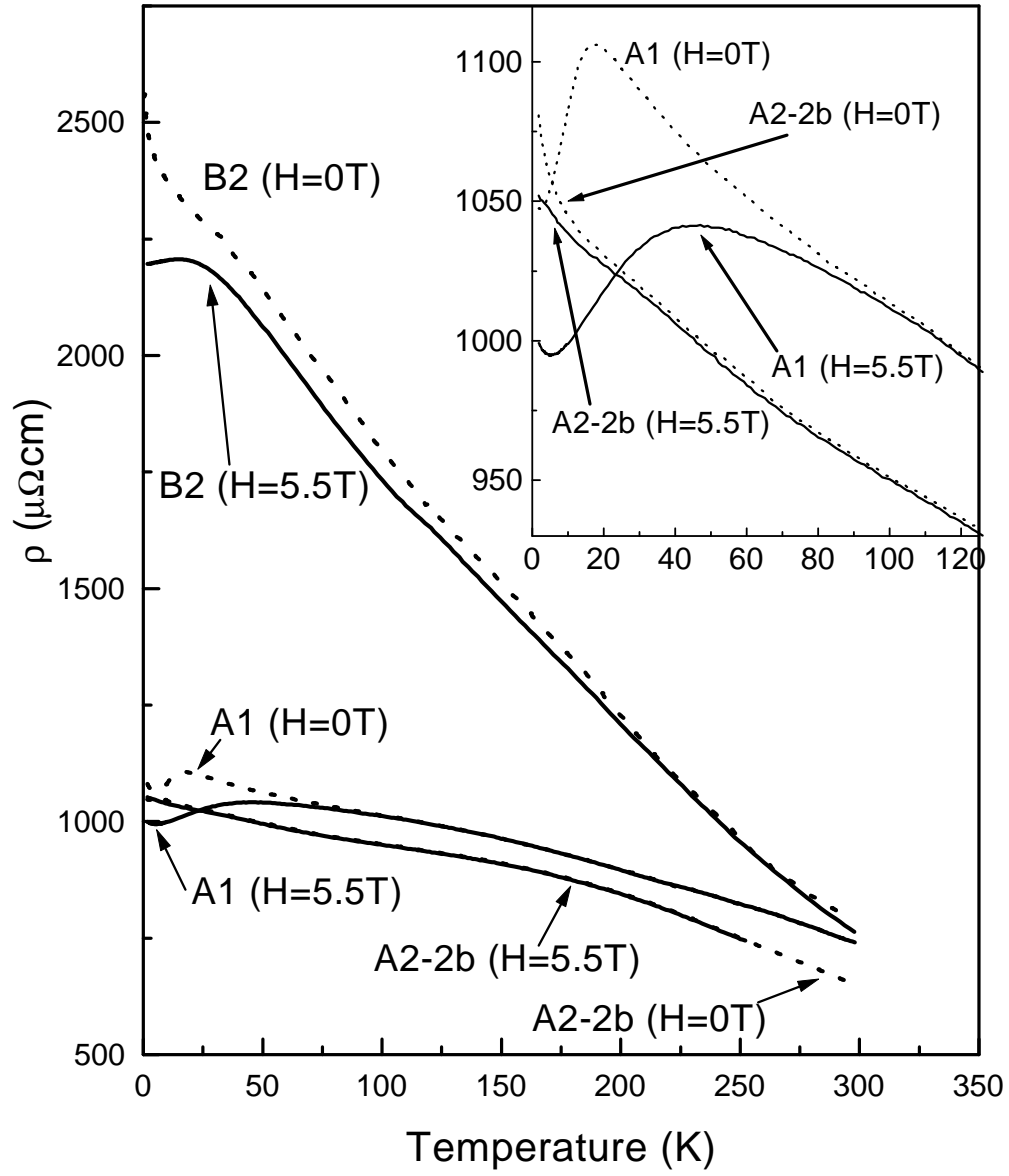
Figure 3.6   Magnetic field dependence of the resistivity of Fe$_2$VAl. The
applied magnetic field is 5.5 T.
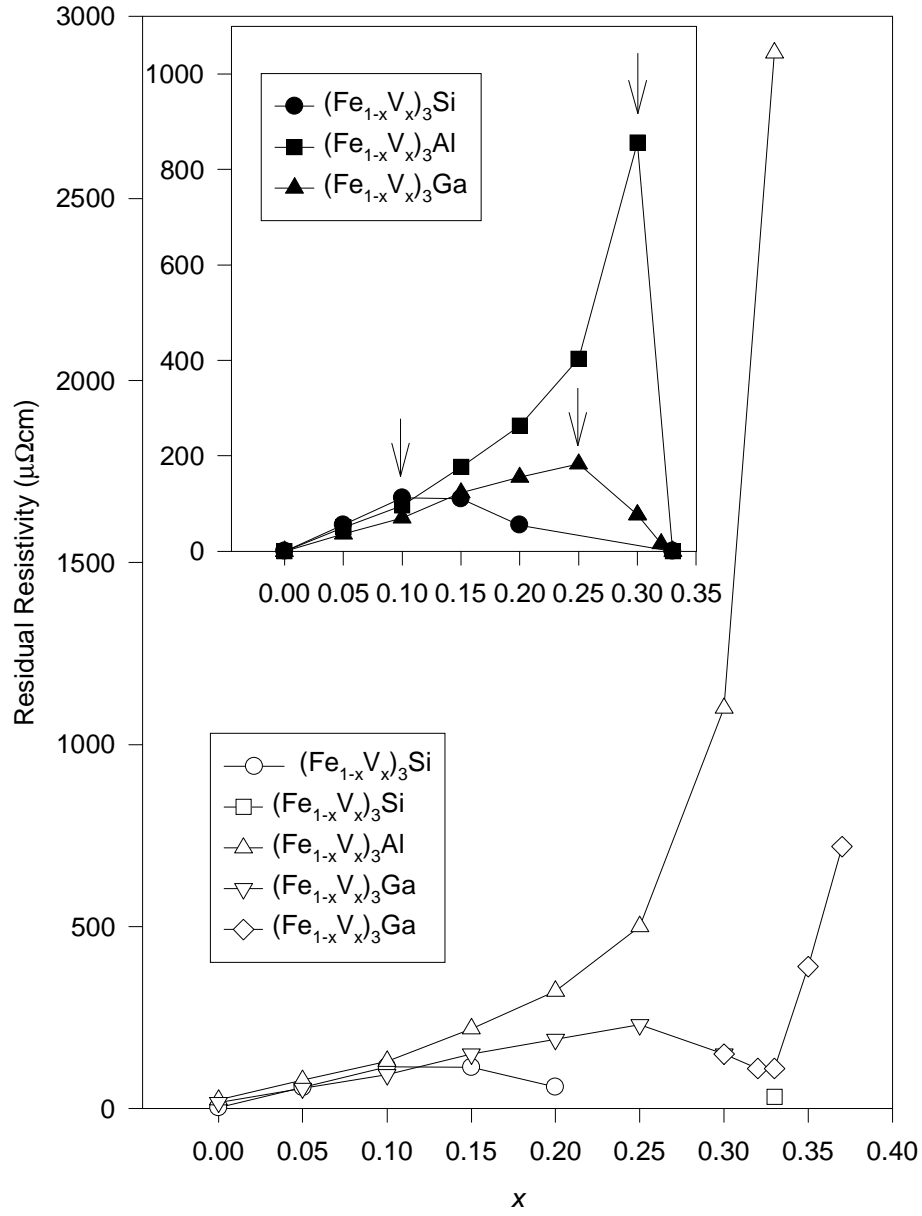
Figure 3.7 Residual resistivities of Heusler alloys $(Fe_{1-x}V_x)_3Ga$ ($\triangledown$: [Kaw1]; $\diamondsuit$: [End1]), $(Fe_{1-x}V_x)_3Si$ ($\bigcirc$: [Nis2]; $\square$: [End2]), and $(Fe_{1-x}V_x)_3$ Al ($\triangle$: [Nis1]). The inset shows residual resistivities with contributions from percolation mixing subtracted.

4   Fe-$3s$ CORE-LEVEL SPLITTING AND LOCAL MAGNETISM IN Fe$_2$VAl

A paper published in Physical Review B [1]

Ye Feng[2], M. V. Dobrotvorska [3], J. W. Anderegg[1], C. G. Olson[1], D. W. Lynch[1]

Abstract

X-ray and soft X-ray photoelectron spectra were taken on Fe$_2$VAl samples. The Fe $3s$ spectra show a shoulder on the higher binding energy side of the main peak, split by ≈ 4.7 eV. Based on current understanding of core-level multiplet splitting in transition-metal compounds, we believe this is direct evidence of a local moment in Fe$_2$VAl.

4.1   Introduction

Fe$_2$VAl was shown recently to have fascinating physical properties[Nis1]. With an enhanced density of states at E_F seen in photoemission and specific-heat measurements, and the negative temperature coefficient of its unusually large resistivity, heavy fermion physics was proposed. There is also evidence contradictory to the ground state of a Kondo lattice. First, $3d$ electrons are more delocalized than their $4f$ counterparts. Significant overlap of the wave functions tends to suppress the Kondo effect, making $3d$ heavy fermions very rare. Two candidates are FeSi[Sch1] and LiV$_2$O$_4$[Kon1]. Second, there is experimental evidence of superparamagnetism in this material, from results of Mössbauer[Pop1], magnetic-field-dependent

---

specific heat[Lue1], and saturation magnetization experiments[Fen2]. *Ab initio* calculations [Guo1,Sin1,Weh1,Ban1], assuming V, Fe, Al, and Fe occupy diagonal sites sequentially in a Heusler structure, gave a *nonmagnetic* ground state with semimetallic band structure. Although most of the theoretical speculations agreed on spin fluctuations as the primary cause of those unusual properties of Fe_2VAl[Guo1,Sin1], not much quantitative understanding was possible because of the lack of experimental data, particularly regarding the magnetic state of this alloy. There were also theoretical speculations that dynamic exciton correlations, which have nothing to do with magnetism, might be responsible for the anomalous physical properties of Fe_2VAl[Weh1]. The valence band of Fe_2VAl has since been studied by resonant photoemission spectroscopy[Sod1]. The partial densities of states found agree very well with those from band-structure calculations, except near the Fermi level. Understanding the magnetism in the ground state is crucial in revealing the physics behind Fe_2VAl.

To comprehend the magnetic structure of Fe_2VAl, we investigated the Fe core-level multiplet splitting by x-ray photoelectron spectroscopy (XPS). The shallow-core-level multiplet splitting due to local magnetic moments was first observed in mostly ionic $3d$ transition metal compounds[Fad1,Fad2]. In the simplest model, this splitting is due to intra-atomic exchange interaction between unpaired 3d electrons and the $3s$ photohole in the final state of the system[Shi1]. Van Vleck's theorem predicts a doublet with separation $\Delta E = (2S+1)G^2(3s,3d)/5$, with $G^2(3s,3d)$ the $3s-3d$ exchange integral, and S the ground-state spin. The intensity ratio in this model is proportional to the ratio of angular momentum multiplicity, $S/(S+1)$. Correlation of the size of the splitting of the $3s$ orbital and the hyperfine field was soon realized in some compounds containing Fe or Mn[Huf1]. Based on these findings, $3s$ multiplet splitting started to be used as a diagnostic tool for local moments[Mcf1]. However, calculations using Hartree-Fock theory, based on the one-electron approximation, yielded too large a splitting and a different intensity ratio, compared to experiments. Bagus, Freeman and Sasaki [Bag1] were the first to realize that intra-atomic configuration interaction of the electrons within the same subshell, largely due to the near degeneracy of the orbital energies of the $3p^2$ and $3s3d$ configurations, causes a significant modification to the final states. By including additional

internal configurations, they were able to account for both the size of the $3s$ splitting and the intensity ratio of the Mn^{2+} compounds. Their prediction of weaker satellite peaks was later verified by experiments[Kow1]. Furthermore, XPS spectra of gaseous Mn and solid-state Mn^{2+} ionic compounds were compared[Her1]. No significant difference was found between them, which further affirms the atomic character of these multiplets. Screening due to charge transfer from ligands was not necessary to produce these multiplets.

The success in understanding Mn^{2+} multiplet splittings lies in the half-filled $3d$ shell. Local screening is suppressed due to a large ligand-to-3d charge-transfer gap. Aside from magnetic insulators with Mn^{2+}, however, the relation between $3s$ splitting and the local magnetic moment is not as straightforward. Studies [Ack1,Fen3] have found that for many metals, metalloids, and nonmetals containing Fe, the splitting of $3s$ levels is not proportional to the local moment measured by neutron scattering, saturation magnetization, or hyperfine fields. In two references[Ohs1,San1], the Anderson Hamiltonian in the impurity approximation was solved, treating exchange splitting, intra-atomic degeneracy and screening by ligands on an equal footing. In both accounts, screening was found to be an integral part of XPS spectra. With increasing atomic number of cations (from Mn) or decreasing electronegativity of ligands, the charge-transfer energy from ligand to $3d$ atom becomes smaller, thereby local screening by the charge-transferred $3d$ electron becomes more likely. A direct extraction of exchange energy from the splitting of the two strongest peaks, without regard to local screening, is unwarranted. Experimentally, if the charge-transfer satellite of the $2p$ core level is small, the major multiplet splitting of $3s$ is still a good measure of the exchange energy[Ohs1], with the intrashell redistribution of electrons only contributing to satellites at much higher energy[Kow1, Vii1].

Recent advances in high-resolution spin-polarized photoemission have made more detailed experiments possible. In separate efforts, three groups [Hil1,See1,Xuz1] have measured the $3s$ splitting of Fe metal. One single peak dominates minority-spin emission at the lower binding energy but two structures were discovered in the majority-spin emission at 0.9 and 4.5 eV higher in binding energy. Although the theoretical modeling[Bag2] of Fe, based on the atomic Fe $3d^7$ ion, gave a fair estimate of the energy separation of the high- and low-spin final states and

also the relative intensities, the origin of the 0.9-eV difference between majority and minority emissions of the high-spin component is still elusive. It is prudent to say that within current understanding, exchange splitting is the cause of the satellite of Fe-3s core level, 4.5 eV below the main peak.

In this work we report the observation of Fe-3s satellite structures in the Heusler-like alloy Fe_2VAl. In conjunction with recent understanding of the multiplet splitting, we propose that this final-state structure is the first signature of local magnetic moments in Fe_2VAl.

4.2   Experiments

The samples involved were grown by the Bridgman method (sample $\mathcal{B}2$), Czochralski method (sample $\mathcal{C}$), and arc melting (samples $\mathcal{A}1$ and $\mathcal{A}2$). Their growth procedure, chemical composition, crystal structure, magnetic and transport properties were described in an earlier paper[Fen2]. It suffices to point out here that most samples are close to stoichiometric Fe_2VAl with various degrees of Fe and Al deficiency, except for $\mathcal{C}$, which is Fe rich. Severe antisite structural disorder was found in all samples by X-ray diffraction. Saturation magnetization measurements at 2 K found at least two kinds of superparamagnetic clusters in samples $\mathcal{A}2$ and $\mathcal{B}2$. $\mathcal{A}1$ and $\mathcal{C}$ were found to have magnetic transitions around 18 and 50 K, respectively.

The XPS spectra at room temperature were taken using a Physical Electronics 5500 Multi-Technique system with monochromatized Al K_α radiation. A hemispherical electron energy analyzer was used. The resolution of the spectrometer (FWHM) was 0.65 eV, with a spot size around 1 $mm \times 1$ mm. The base pressure of the XPS system was less than 7×10^{-10} Torr, and 4×10^{-10} Torr in the preparation chamber. We have also taken spectra using 150-eV synchrotron radiation at the Synchrotron Radiation Center. With a slit width of 70 μm on a 2-m ERG monochromator and pass energy of the electron analyzer of 50 eV, a comparable resolution was achieved at the Ames-Montana beamline. Pressure of this UHV system is 5×10^{-11} Torr.

The XPS data-analysis package was used to obtain the atomic concentrations. Corrections due to the photoionization cross section of atomic shells, electron escape depth, transmission

function of the electron analyzer, and detection angle had been applied. The atomic percentage is obtained by integrating C-1s, O-1s, Al-2p, V-2p and Fe-2p photoelectrons.

Fracturing the samples *in situ* is found to yield surfaces with least oxygen and carbon content. Using inert gas etching or *in-situ* grinding to clean sample surfaces were not proper procedures. During argon-ion bombardment preferential sputtering of the lightest element (Al) was observed. After grinding with a diamond wheel several times, large amounts of oxide and carbon remained on the surface. We chose to break the samples *in situ*. There was always 5 at.% oxygen contamination right after fresh surfaces of Fe_2VAl were uncovered. When these surfaces were further exposed to oxygen, aluminum oxide quickly formed to become the major oxide on the surface. Even with vacuum as good as 5×10^{-11} Torr, aluminum oxide showed up as a distinct shoulder in the Al-2p spectrum 24 h after cleavage. Intensive argon-ion sputtering of the fractured surface of sample $\mathcal{A}2$ yielded about 3 at.% oxygen remaining. Fe and V oxide formation as evidenced by the change of slope at the higher-binding energy side of the 2p peaks were less obvious and were detected only after aluminum oxide peaks were evident. Surface carbon content right after cleaving was less than 4 at.% for all samples except $\mathcal{A}2$, which had almost 9 at.%. We found regularly two peaks associated with the carbon 1s orbital. The one with binding energy near 285 eV changed with surface conditions. Associated with the C-H bond, this peak diminished to zero with sputtering but regained its intensity after time in vacuum. The other peak at 283-eV binding energy was identified to be from carbide bonding. This carbide peak gained some intensity in the middle of the sputtering, similar to the carbide formation on the TiFe surface activated by ion bombardment[Sel1]. Terminal carbon intensity in sample $\mathcal{A}2$ is around 3 at.%. Carbon concentration at this level was found to bear no relation to the core-level spectra of any other element. Still, the carbon and aluminum (oxide) peaks were checked during the integration of the Fe-2p and Fe-3s data to insure that there was no detectable contamination. All spectra discussed in the following were taken right after cleavage, without sputtering and before aluminum oxide appeared. The composition of Fe, V, and Al on these surfaces was compared to the stoichiometries measured by atomic emission spectroscopy[Fen2]. The relative atomic ratios are consistent with each other. Therefore,

the electronic and magnetic properties of the *in-situ* fractured surfaces are regarded to be representative of the bulk.

4.3   Results and Discussion

Fe $2p$ and Fe-$3s$ spectra of all Fe_2VAl samples, together with that of pure Fe, are shown in Figs. 4.1 and 4.2. The Fe-$3p$ spectrum of sample $\mathcal{A}2$ was taken at 150-eV photon energy with better vacuum, and that of pure Fe was taken with Al K_α excitation. They are shown in Fig. 4.3. All spectra have been normalized to a peak intensity of 100 and displaced relatively for ease of viewing. With only one spin-orbit doublet, none of the Fe $2p$ spectra have extra peaks due to chemical shifts or plasmon excitations. Without any satellite structure in the $2p$ or $3p$ spectra, we can also rule out the importance of local versus nonlocal screening. The lesser asymmetry of Fe_2VAl peaks, relative to that of Fe, observed in all core levels hints at the suppressed electron-hole pair excitations near E_F in Fe_2VAl samples. All $3s$ spectra have shoulders around 5 eV below the main peak.

In the case of Fe, spin-polarized photoemission[Hil1,See1,Xuz1] reveals the existence of three peaks. With our experimental resolution comparable to the smallest separation of these peaks, we cannot fit all three peaks and perform line-shape analysis. However, we can still compare Fe_2VAl with Fe, in the spirit of Refs. [Ack1] and [Qiu1]. For each $3s$ spectrum, a Shirley background[Shi1] was subtracted first and the remainder was fit with two peaks of Doniach-Šunjić (DS) line-shape[Don1]. The standard deviations of each parameter were obtained in the least-square Marquardt-Levenberg fitting. Relevant parameters of this fitting and selected literature results are given in Table 4.1. The difference of our fitting results and those of Ref. [Ack1] for pure Fe is primarily due to the Shirley background subtraction and the independence of α_1 and α_2 in our fittting. Although the asymmetry parameter α depends on the shape of the density of states near E_F and would allow us to obtain more information[Don1], it was recognized that the interference of the nearby majority-spin emission alters the apparent α of the main peak[See1]. I_1/I_2 is strongly affected also.

As shown in the Table 4.1, all Fe-$3s$ splitting parameters are very similar, although the

saturation moment varies by an order of magnitude. All samples show a secondary peak with considerable intensity 4.7 eV below the main peak. This is very similar to the case of pure Fe. Assuming the proportionality of exchange splitting and $2S + 1$ still applies, this secondary peak provides evidence that a large fraction of the Fe atoms in Fe_2VAl carry a local moment of around 2.2 μ_B. Singh and Mazin[Sin1] found that although Fe_2VAl in the ordered $L2_1$ phase will have no moment on the Fe atoms, the local moment on antisite Fe atoms is very robust, always 2.2 -2.3 μ_B. These XPS spectra therefore confirm the large amount of antisite structural disorder found in these alloys[Fen2]. The small saturation moments at low temperature do not necessarily contradict the large relative intensity of the satellite. Our study of Fe_2VAl [Fen1] has found not only two types of superparamagnetic clusters composed of magnetic antisite Fe atoms, but more anti-site Fe atoms that are probably locked in a spin-glass state. The Fe atoms in superparamagnetic clusters give a small saturation moment of 0.02-0.37 μ_B/f.u. at 2 K, probably even less at elevated temperatures. However, all Fe atoms, including those in the spin-glass state, should carry a local moment and contribute to the intensity of the satellite.

In summary, our Fe-3s spectra show that a large number of Fe atoms in Fe_2VAl are in antisite disorder. Each one carries a moment of 2.2 μ_B. Further spin-polarized photoelectron experiments should clarify the details.
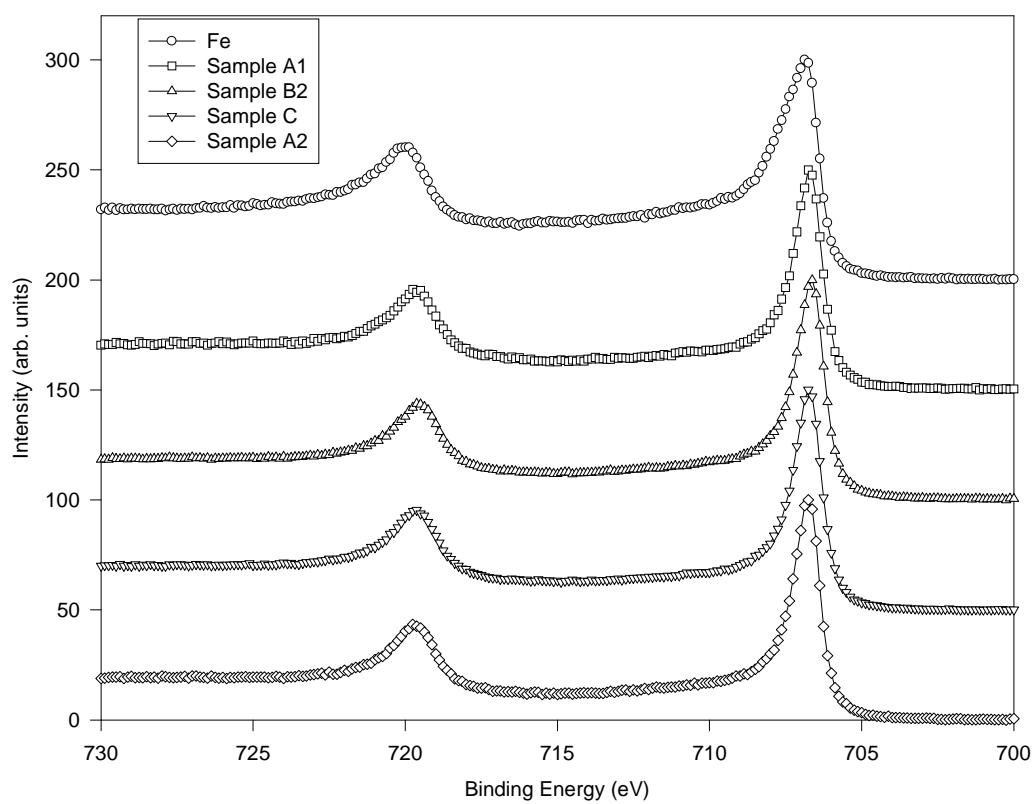
Acknowledgments

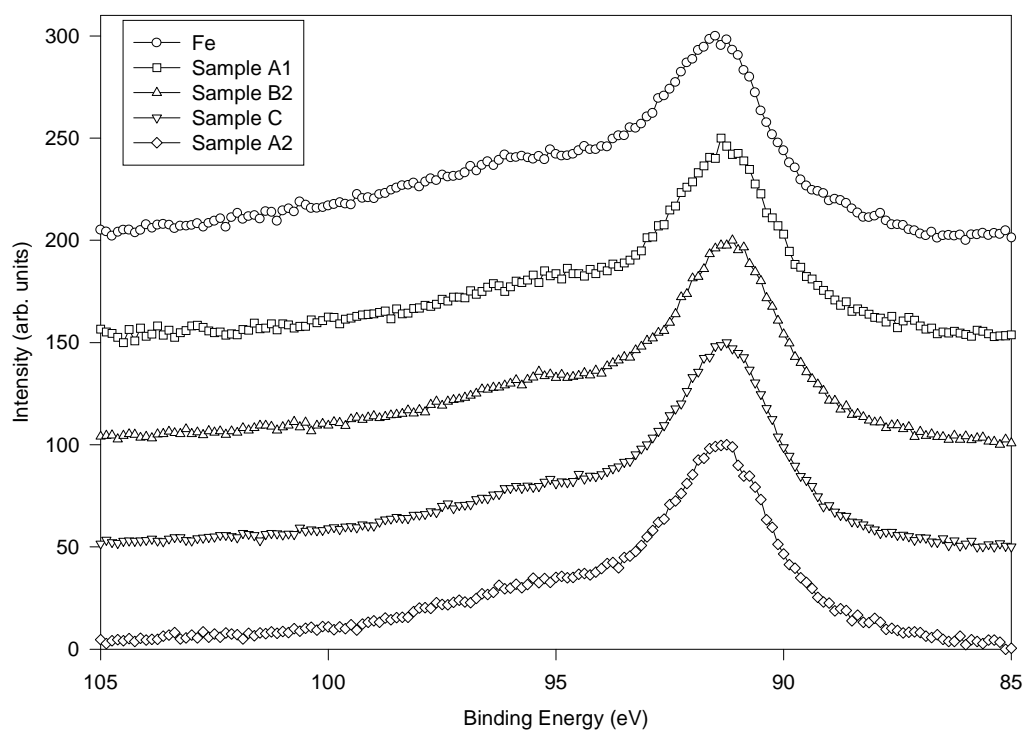Figure 4.1   Experimental Fe-2p spectra. Photon energy is 1487 eV.

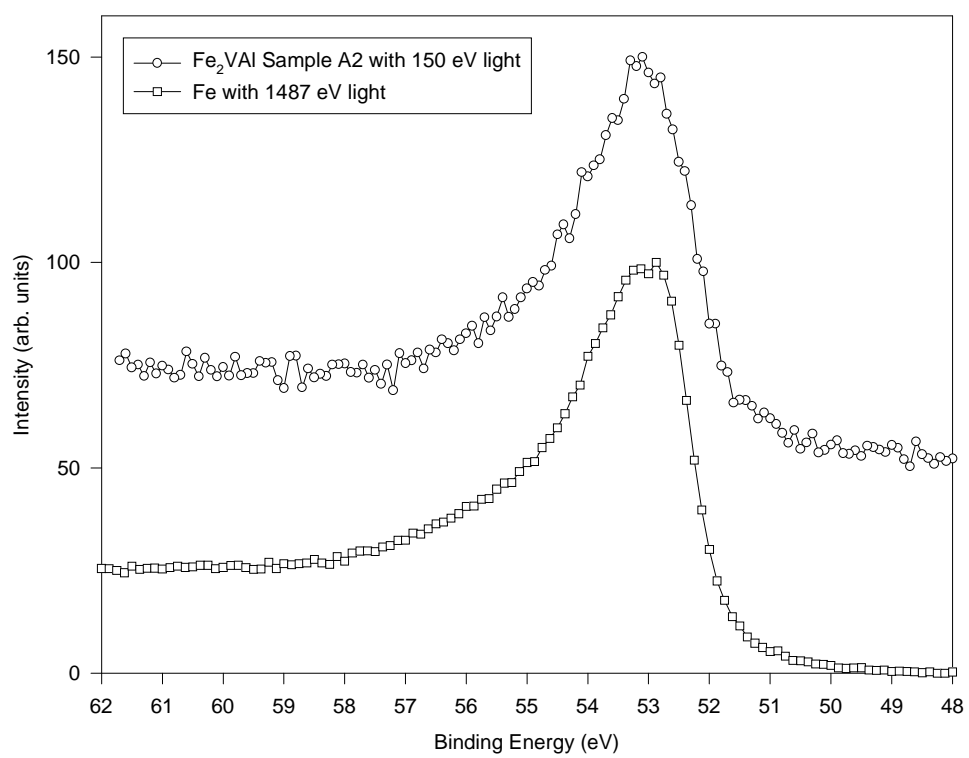Figure 4.2   Experimental Fe-3s spectra. Photon energy is 1487 eV.

Figure 4.3   Experimental Fe-3*p* spectra.

Table 4.1 Comparison of line shape parameters of Fe $3s$ spectra and magnetic moments in Fe$_2$VAl and pure Fe. γ_1 and γ_2 are the Lorentzian widths of the main and satellite peaks. α_1 is the asymmetry parameter of the DS line shape of the main peak. $\alpha_2 \approx 0$ in all fittings. I_1/I_2 is ratio of integrated intensities. μ is the saturation moment measured at 2 K.

Sample	ΔE (eV)	γ_1 (eV)	γ_2 (eV)	α_1	I_1/I_2	μ (μ_B/f.u.)
σ^a	0.2	0.02	0.2	0.01	-	-
$\mathcal{B}2$	4.7	1.27	2.0	0.13	5.4	0.05
$\mathcal{C}$	4.7	1.23	2.3	0.13	5.4	0.33
$\mathcal{A}1$	4.6	1.27±0.03	2.3±0.3	0.10±0.02	4.1	0.37
$\mathcal{A}2$	4.6	1.25	2.3	0.13	5.1	0.02
Fe	4.9±0.3	1.20±0.03	3.4±0.3	0.15±0.02	2.3	2.2
Fe [Qiu1]^b	4.8			0.19	3.0	2.2
Fe [Ack1]^c	4.9	1.1	1.3-1.8	0.27	4.5	2.2

^{a}standard deviation of our fitting, unless otherwise indicated.
^{b}Mg K_α used; linear background subtraction; α_2=0.08.
$^c\alpha_1$=α_2 forced; no background corrections.

5 CONCLUSION

We found three papers that are extremely helpful in supporting the dominance of antisite disorder in Fe_2VAl. They are going to be reviewed in more details before we reach the final conclusion.

The first paper is by Popiel *et al.*, reporting the first synthesis of $Fe_{3-x}V_xAl$ with $0 < x < 1.1$ [Pop1]. Through their XRD analysis, the existence of antisite disorder was identified. Their Mössbauer experiments were similar to our XPS experiment, both probing local magnetic moments. However, around the Fe_2VAl composition, it was not possible to read from the Mössbauer spectra how much antisite disorder there was. Another significant contribution of this article is the recognition of a ferromagnetism-to-superparamagnetism transition. In the XRD and magnetization sections in chapter III, we basically reach the same conclusion as this paper, albeit different in details.

Another experimental paper of great importance is published by Matsuda *et al.* [Mat2]. Our resistivity data have great resemblance to their data, especially in the magnetic field. However, we disagree on the explanation of resistivity in the low temperature range. Matsuda *et al.* described it to be of variable-range hopping but we found that the fitting in that range is quite arbitrary, and also the resistivity in that range depends on the external magnetic field. Their spontaneous magnetization is larger than ours probably because their samples are further away in stoichiometry than ours, as indicated by the Curie temperatures. Nonetheless, we agree on the formation of magnetic clusters due to atomic disorders.

The theoretical paper by Singh and Mazin [Sin1] had a strong emphasis on spin fluctuations in Fe_2VAl due to antisite disorder. The supercell method was employed in the LMTO calculations to calculate the resultant magnetic clusters. It is found that when Fe is placed

into the nominal V site and coordinated with eight transition metals as nearest neighbors, its crystal field splitting is larger than the widths of the e_g and t_{2g} subband and therefore the Fe atom is intrinsically magnetic. This property is independent of the redistribution of Fe and V in the transition-metal sublattice and even independent of the changes of the V concentration. Although the small density of states at E_F does not favor a Stoner instability, the formation of magnetic clusters due to antisite disorder is very robust. The authors also pointed out that in this system, the RKKY interaction with long wavelength modulations (due to small carrier density) is also modulated by the wavevector characterizing the *separation* of two patches of the Fermi surfaces. Therefore, spin-glass behavior with nearest-neighbor magnetic moments randomly oriented is favored. Given all the above, they suggested most of the physical properties of Fe_2VAl are determined by the local moments interacting with low-density carriers. Their predictions are marvelously accurate when compared with our experiments.

In summary, we have found this material to have multiple phases. These phases exhibit themselves in the x-ray diffraction pattern. Magnetically, superparamagnetism due to magnetic clusters and other local magnetism (maybe either antiferromagnetism or spin-glass) are caused by the disordered Fe atoms. The definite signature of local magnetic moments comes from our saturation magnetization and core-level multiplet splitting measurements. FeVFeAl may contribute to the weak Pauli paramagnetism due to the low density of carriers. The electronic structure can also be understood well with the separation of phases. The large density of states as seen in specific-heat coefficient and photoemission is primarily due to the growth of band-tail states with lattice disorder. The fact that E_F falls right into the "localization valley" explains the seemingly semiconducting resistivity. However, only the itinerant carriers can follow the IR frequency to give free-electron plasma oscillations. In the end, this sample is very sensitive to the preparation conditions, especially annealing. We have found strong theoretical support to our findings.

There are some lingering questions as to what kind of local magnetism there is in Fe_2VAl. If it were antiferromagnetism or spin-glass, one would normally align the moments with a large enough field. Probably further magnetization experiments can be done to clarify this.

We think most of the controversy around Fe_2VAl can put to rest. A detailed theoretical treatment with disordered magnetic system interacting with (low density) carrier may help explain why for most part of the resistivity curve, a linear relation is found. The same linear curve is found in Mooij's paper [Moo1]. However, the sensitivity of Fe_2VAl to preparation conditions gives a lot of noise to the true physical signature of this system. Considerable difficulty is forseen in the next level of research.

BIBLIOGRAPHY

[Ack1] J. F. van Acker, Z. M. Stadnik, J. C. Fuggle, H. J. W. M. Hoekstra, K. H. J. Buschow, G. Stroink, Phys. Rev. B **37**, 6827 (1988).

[And1] O. K. Andersen, Phys. Rev. B **12**, 3060 (1975).

[And2] O. K. Andersen and O. Jepsen, Phys. Rev. Lett. **53**, 2571 (1984).

[Ans1] V. I. Anisimov, S. Yu Ezhov, I. S. Elfimov, I. V. Solovyev, and T. M. Rice, Phys. Rev. Lett. **76** 1735 (1996).

[Bag1] P. S. Bagus, A. J. Freeman and F. Sasaki, Phys. Rev. Lett. **30**, 850 (1973).

[Bag2] P. S. Bagus and J. V. Mallow, Chem. Phys. Lett. **228**, 695 (1994).

[Ban1] A. Bansil, S. Kaprzyk, P. E. Mijnarends, and J. Tobola, Phys. Rev. B **60**, 13396 (1999).

[Ber1] G. Bergmann, Phys. Rev. B **28**, 2914 (1983).

[Bra1] A. J. Bradley and A. H. Jay, Proc. Roy. Soc. London **A136**, 210 (1932).

[Che1] M. A. Chernikov, L. Degiorgi, E. Felder, S. Paschen, A. D. Bianchi, H. R. Ott, J. L. Sarrao, Z. Fisk, and D. Mandrus, Phys. Rev. B **56**, 1366 (1997).

[Dit1] J. F. DiTusa, K. Friemelt, E. Bucher, G. Aeppli, and A. P. Ramirez, Phys. Rev. B **58**, 10288 (1998).

[Don1] S. Doniach and M. Šunjić, J. Phys. C **3**, 285 (1970).

[End1] K. Endo, H. Matsuda, K. Ooiwa, M. Iijima, T. Goto, K. Sato, and I. Umehara, J. Magn. Magn. Mater. **177-181**, 1437 (1998).

[End2] K. Endo, H. Matsuda, K. Ooiwa, and K. Itoh, J. Phys. Soc. Jpn. **64**, 2329 (1995).

[End3] K. Endo, H. Matsuda, K. Ooiwa, M. Iijima, K. Ito, T. Goto and A. Ono, J. Phys. Soc. Jpn. **66**, 1257 (1997).

[Fad1] C. S. Fadley, D. A. Shirley, A. J. Freeman, P. S. Bagus, and J. V. Mallow, Phys. Rev. Lett. **23**, 1397 (1969).

[Fad2] C. S. Fadley and D. A. Shirley, Phys. Rev. A **2**, 1109 (1970).

[Fat1] W. G. Fateley, F. R. Dollish, N. T. McDevitt, and F. F. Bentley, *Infrared and Raman Selection Rules for Molecular and Lattice Vibrations: The Correlation Method.* (John Wiley & Sons, New York, 1972).

[Fen1] Ye Feng, C. Ambrosch-Draxl, J. M. Park, A. J. Sievers, C. G. Olson, D. W. Lynch, to be published.

[Fen2] Ye Feng, *et al.* (Charpter 3)

[Fen3] It is worth noting that $NbFe_2$, one of the alloys designated as a Pauli paramagnet but with an Fe $3s$ shoulder in XPS spectra in [Ack1], was recently shown to exhibit both ferromagnetic and antiferromagnetic spin fluctuations (Y. Yamada, A. Sakata, and T. Murakami, J. Phys. Soc. Japan **62** 1710 (1993)). If these local moments remain stable at room temperature, they would show up in Fe $3s$ multiplet splitting.

[Fre1] A. J. Freeman, P. S. Bagus, and J. V. Mallow, Int. J. Magn. **4**, 35 (1973).

[Fuc1] C. Fu, M. P. C. M. Krijn and S. Doniach, Phys. Rev. B **49**, 2219 (1994).

[Fuc2] C. Fu and S. Doniach, Phys. Rev. B **51** 17439 (1995).

[Fuj1] S. Fujii, S. Sugimura, S. Ishida, and S. Asano, J. Phys.: Condens. Matter **2**, 8583 (1990).

[Fuj2] H. Fujii, H. Kawanaka, T. Takabatake, M. Kurisu, Y. Yamaguchi, J. Sakurai, H. Fujiwara, T. Fujita and I. Oguro, J. Phys. Soc. Jpn. **58**, 2495 (1989).

[Ful1] B. Fultz, T. A. Stephens, W. Sturhahn, T. S. Toellner, and E. E. Alp, Phys. Rev. Lett. **80**, 3304 (1998).

[Guo1] G. Y. Guo, G. A. Botton, and Y. Nishino, J. Phys.: Condens. Matter **10**, L119 (1998).

[Gro1] R. A. de Groot, F. M. Mueller, P. G. van Engen, and K. H. J. Buschow, Phys. Rev. Lett. **50**, 2024 (1983).

[Her1] B. Hermsmeier, C. S. Fadley, M. O. Krause, J. Jimenez-Mier, P. Gererd, and S. T. Manson, Phys. Rev. Lett. **61**, 2592 (1988).

[Hil1] F. U. Hillebrecht, R. Jungblut, and E. Kisker, Phys. Rev. Lett. **65**, 2450 (1990).

[Huf1] S. Hüfner and G. K. Wertheim, Phys. Rev. B **7**, 2333 (1973).

[Hun1] M. B. Hunt, M. A. Chernikov, E. Felder, H. R. Ott, Z. Fisk, and P. Canfield, Phys. Rev. B **50**, 14933 (1994).

[Ish1] S. Ishida, J. Ishida, S. Asano, and J. Yamashita, J. Phys. Soc. Jpn. **41**, 1570 (1976).

[Jar1] T. Jarlborg, Phys. Rev. B **51** 11106 (1995).

[Jar2] T. Jarlborg, Phys. Rev. B **59** 15002 (1999).

[Kat1] M. Kato, Y. Nishino, U. Mizutani, and S. Asano, J. Phys.:Condens. Matter **12**, 1769 (2000).

[Kaw1] N. Kawamiya, Y. Nishino, M. Matsuo, and S. Asano, Phys. Rev. B **44**, 12406 (1991).

[Kaw2] N. Kawamiya, K. Adachi, J. Magn. Magn. Mater. **31-34**, 145 (1982).

[Kon1] S. Kondo, D. C. Johnston, C. A. Swenson, F. Borsa, A. V. Mahajan, L. L. Miller, T. Gu, A. I. Goldman, M. B. Maple, D. A. Gajewski, E. J. Freeman, N. R. Dilley, R. P. Dickey, J. Merrin, K. Kojima, G. M. Luke, Y. J. Uemura, O. Chmaissem, and J. D. Jorgensen, Phys. Rev. Lett. **78**, 3729 (1997).

[Kow1] S. P. Kowalczyk, L. Ley, R. A. Pollak, F. R. McFeely, and D. A. Shirley, Phys. Rev. B **7**, 4009 (1972).

[Kud1] J. Kudrnovsky, N. E. Christensen, and O. K. Andersen, Phys. Rev. B **43**, 5924 (1991).

[Lue1] C. S. Lue, J. H. Ross, Jr., C. F. Chang, and H. D. Yang, Phys. Rev. B **60**, R13941 (1999).

[Man1] D. Mandrus, J. L. Sarrao, A. Migliori, J. D. Thompson, and Z. Fisk, Phys. Rev. B **51**, 4763 (1995).

[Mat1] A. Matsushita and Y. Yamada, J. Magn. Magn. Mater. **196-197**, 669 (1999).

[Mat2] H. Matsuda, K. Endo, K. Ooiwa, M. Iijima, Y. Takano, H. Mitamura, T. Goto, M. Tokiyama and J. Arai, J. Phys. Soc. Jpn. **69**, 1004 (1999).

[Mat3] L. F. Mattheiss and D. R. Hamann, Phys. Rev. B **47**, 13114 (1993).

[Mcf1] F. R. McFeely, S. P. Kowalczyk, L. Ley, and D. A. Shirley, Solid State Commun. **15**, 1051 (1974).

[Moo1] J. H. Mooij, Phys. Status Solidi A **17**, 521 (1973).

[Mot1] N. F. Mott, *Metal-Insulator Transitions,* 2nd ed. (Taylor & Francis, London, 1997).

[Mui1] W. B. Muir, J. I . Budnick, and K. Raj, Phys. Rev. B **25**, 726 (1982).

[Nic1] V. A. Niculescu, T. J. Burch, and J. I. Budnick, J. Magn. Magn. Mater. **39**, 223 (1983), and references therein.

[Nis1] Y. Nishino, M. Kato, S. Asano, K. Soda, M. Hayasaki, and U. Mizutani, Phys. Rev. Lett. **79**, 1909 (1997).

[Nis2] Y. Nishino, S. Inoue, S. Asano, and N. Kawamiya, Phys. Rev. B **48**, 13607 (1993).

[Nis3] Y. Nishino, C. Kumada and S. Asano, Scr. Mater. **36**, 361 (1997).

[Nis4] Y. Nishino, M. Matsuo, S. Asano, and N. Kawamiya, Scr. Metall. Mater. **25**, 2291 (1991).

[Nol1] G. Nolze, private communication.

[Ohs1] S. J. Oh, G. H. Gweon, and J. G. Park, Phys. Rev. Lett. **68**, 2850 (1992).

[Oht1] H. Ohta, S. Kimura, E. Kulatov, S. V. Halilov, T. Nanba, M. Motokawa, M. Sato, and K. Nagasawa, J. Phys. Soc. Jpn. **63** 4206 (1994).

[Oka1] H. Okamura, J. Kawahara, T. Nanba, S. Kimura, K. Soda, U. Mizutani, Y. Nishino, M. Kato, I. Shimoyama, H. Miura, K. Fukui, K. Nakagawa, H. Nakagawa, and T. Kinoshita, Phys. Rev. Lett. **84**, 3674 (2000).

[Okp1] D. E. Okpalugo, J. G. Booth, and C. A. Faunce, J. Phys. F:Met. Phys **15**, 681 (1985).

[Opp1] P. M. Oppeneer, A. N. Yaresko, A. Ya. Perlov, V. N. Antonov and H. Eschrig, Phys. Rev. B **54**, R3706 (1996).

[Pas1] S. Paschen, E. Felder, M. A. Chernikov, L. Degiorgi, H. Schwer, H. R. Ott, D. P. Young, J. L. Sarrao, and Z. Fisk, Phys. Rev. B **56**, 12916 (1997).

[Pop1] E. Popiel, M. Tuszynski, W. Zarek, and T. Rendecki, J. Less-Common Met. **146**, 127 (1989).

[Qiu1] S. L. Qiu, R. G. Jordan, A. M. Begley, X. Wang, Y. Liu, and M. W. Ruckman, Phys. Rev. B **46**, 13004 (1992).

[Ris1] P. S. Riseborough, Phys. Rev. B **58** 15534 (1998).

[San1] L. Sangaletti, L. E. Depero, P. S. Bagus, F. Parmigiani, Chem. Phys. Lett. **245**, 463 (1995).

[Sch1] Z. Schlesinger, Z. Fisk, H.-T. Zhang, M. B. Maple, J. F. DiTusa, and G. Aeppli, Phys. Rev. Lett. **71**, 1748 (1993).

[See1] A. K. See and L. E. Klebanoff, Phys. Rev. B **51**, 7901 (1995).

[Sel1] P. Selvam, B. Viswanathan and V. Srinivasan, J. Less-Common Met. **161**, 77 (1990).

[Shi1] D. A. Shirley, in *Photoemission in Solids I*, M. Cardona and L. Ley, eds. (Springer-Verlag, Berlin, 1978) p. 165.

[Shi2] D. A. Shirley, Phys. Rev. B **5**, 4709 (1972).

[Sin1] D. J. Singh and I. I. Mazin, Phys. Rev. B **57**, 14352 (1998).

[Sod1] K. Soda, T. Takeuchi, Y. Yanagida, U. Mizutani, M. Kato, Y. Nishino, A. Sekiyama, S. Imada, S. Suga, T. Matsushita, and Y. Saito, Jpn. J. Appl. Phys. **38**, 496 (1999) Suppl. 38-1.

[Tak1] Y. Takahashi, J. Phys.: Condens. Matter **9**, 2593 (1997).

[Tal1] E. Talik, J. Szade, J. Heimann, A. Winiarski, A. Winiarska, K. Majewska, and A. Chelkowski, J. of Crystal Growth **102**, 187 (1990).

[Tsu1] C. C. Tsuei, Phys. Rev. Lett. **57**, 1943 (1986); C. C. Tsuei, in *Anderson Localization*, T. Ando and H. Fukuyama, eds. (Springer-Verlag, Heidelberg, 1988) p. 143.

[Ull1] K. Ullakko, J. K. Huang, C. Kantner, R. C. O'Handley and V. V. Kokorin, Appl. Phys. Lett. **69** (1996).

[Vii1] E. K. Viinikka and Y. Öhrn, Phys. Rev. B **11**, 4168 (1975).

[Web1] P. J. Webster and K. R. A. Ziebeck, Phys. Lett. **98A**, 51 (1983).

[Weh1] R. Weht and W. E. Pickett, Phys. Rev. B **58**, 6855 (1998).

[Xuz1] Z. Xu, Y. Liu, P. D. Johnson, B. Itchkawitz, K. Randall, J. Feldhaus, and A. Bradshaw, Phys. Rev. B **51**, 7912 (1995).

[Zar1] W. Zarek, E. Talik, J. Heimann, M. Kulpa, A. Winiarska, and M. Neumann, J. Alloys Compd. **297(1-2)**, 53 (2000).

[Zim1] R. Zimmermann, P. Steiner, R. Claessen, F. Reinert, S. Hufner, J. of Electron Spectr. and Related Phen. **96**, 179 (1998).

ACKNOWLEDGEMENTS

My deepest appreciation goes to my advisor Dr. Dave W. Lynch. The tremendous trust that he gave to me in managing this project was overwhelming in the early stage. But with this trust and his generous support, this physics project turned into a great lesson of learning how to initiate a project, how to collaborate with other people and take responsibilities, how to respect other people, and how to react to failures and successes. At the same time, he sets a high standard by example, of not only scholastic excellence but also being very kind to other people. I truly appreciate these five fortunate years of being in his group.

I wish to thank Dr. Cliff Olson for all the guidance and assistance with experiments, and especially for showing me how to meticulously treat experimental details. I am very much indebted to Dr. Joo-Yull Rhee. His help came at the most needed moment of the project. I would also like to thank Dr. Claudia Ambrosch-Draxl, Mr. Jim Anderegg, Dr. Vladimir Antropov, Dr. Sergei Budko, Dr. Paul Canfield, Dr. Maria Dobrotvorska, Dr. Kwang-Joo Kim, Dr. Rudy Lange, and Dr. Seong-Jae Lee for very enlightening discussions throughout these years. I am very appreciative of Mr. Joongmok Park for taking care of our computers and friendly disagreements on a lot of work-related issues.

I am deeply grateful to my wife Li Zheng for her understanding and support in the face of the conflicts between my work and our family time. I want thank my parents for fostering my scientific curiosity when I was young. They are also very good at assuring me that not being able to get good grades is fine. Lastly, I want to extend my appreciation to Mr. Xunya Jiang for his patient explanations of numerous theoretical concepts, continuous encouragement over these five years, and friendship.

This work was performed at Ames Laboratory under Contract No. W-7405-ENG-82 with

the U.S. Department of Energy. The United States government has assigned the DOE report number IS-T 1903 to this thesis.